

Gradient-based topology optimization of soft dielectrics as tunable phononic crystals

Atul Kumar Sharma^a, Majd Kosta^c, Gal Shmuel^b, Oded Amir^c

^a*Department of Mechanical Engineering, Indian Institute of Technology Jodhpur, Jodhpur 342037, India*

^b*Faculty of Mechanical Engineering, Technion–Israel Institute of Technology, Haifa 32000, Israel*

^c*Faculty of Civil and Environmental Engineering, Technion–Israel Institute of Technology, Haifa 32000, Israel*

Abstract

Dielectric elastomers are active materials that undergo large deformations and change their instantaneous moduli when they are actuated by electric fields. By virtue of these features, composites made of soft dielectrics can filter waves across frequency bands that are *electrostatically tunable*. To date, to improve the performance of these adaptive phononic crystals, such as the width of these bands at the actuated state, metaheuristics-based topology optimization was used. However, the design freedom offered by this approach is limited because the number of function evaluations increases exponentially with the number of design variables. Here, we go beyond the limitations of this approach, by developing an efficient gradient-based topology optimization method for maximizing the width of the band gaps in an exemplary case study. We employ a finite element formulation of the governing equations, and use the properties of each element as the design variables. In order to iteratively update the design variables, we employ gradient-based optimization, namely the Method of Moving Asymptotes. We carry out and implement fully analytical sensitivity analysis for computing the gradient of the objective function with respect to each one of the design variables. The numerical results of the method developed here demonstrate prohibited frequency bands that are indeed wider than those that were generated using metaheuristics-based topology optimization, while the computational cost to identify them is reduced by orders of magnitude.

Keywords: Dielectric elastomers, nonlinear electroelasticity, wave propagation, band gaps, composites, Bloch-Floquet waves, gradient-based topology optimization

1. Introduction

Dielectric elastomers (DEs) are active materials that undergo large deformations when they are actuated by electric fields (Pelrine et al., 2000; Hajiesmaili & Clarke, 2021). Moreover, the constitutive relations of DEs are nonlinear, such that their instantaneous moduli vary as functions of the electromechanical loads. These features have led to the design of various applications, such as haptic devices (Kim et al., 2016), soft robots (Gu et al., 2018), actuators (Hajiesmaili & Clarke, 2021; Sharma et al., 2018, 2019; Su et al., 2018, 2019; Kashyap et al., 2020; Sharma et al., 2017;

Email addresses: atulksharma@iitj.ac.in (Atul Kumar Sharma), majd-costa@campus.technion.ac.il (Majd Kosta), meshmuel@technion.ac.il (Gal Shmuel), odedamir@technion.ac.il (Oded Amir)

8 Ortigosa et al., 2021; Ortigosa & Martínez-Frutos, 2021; Khurana et al., 2021) and artificial muscles
9 (Lu et al., 2016), that are based on DEs.

10 More recently, the potential of DEs to function as adaptive waveguides has been explored (Zhu
11 et al., 2020; Mohajer et al., 2021; Jandron & Henann, 2018; Ziser & Shmuel, 2017; Wang et al.,
12 2020; Zhu et al., 2020). These studies are based on the understanding that the physical properties
13 that govern elastic waves are electrostatically tunable. Following the pioneering work of Gei et al.
14 (2011) on *flexural* waves, in a series of papers, Shmuel and collaborators (Shmuel & Debotton,
15 2012; Shmuel, 2013; Shmuel & Pernas-Salomón, 2016; Getz et al., 2017; Getz & Shmuel, 2017;
16 Bortot & Shmuel, 2017) have integrated this concept of material tunability with the theory of
17 *acoustic* band structure, in order to design adaptive wave suppressors. Band theory predicts that
18 waves in elastic composites (also termed phononic crystals) cannot propagate at certain frequencies
19 (band gaps) owing to Bragg reflections, that are functions of the periodicity and the impedance
20 mismatch of the phases (Kushwaha et al., 1993, 1994; Yang & Kim, 2018; Zhang & Gao, 2018;
21 Ren et al., 2020). In addition to this wave isolation characteristic in the band gap frequency region,
22 the phononic crystals with local resonators also exhibit the fracture resistance and crack-arrest
23 characteristics which enhance the strength of the structure (Huang et al., 2020, 2021). The idea to
24 the band gaps using DEs is simple: by applying a bias electromechanical field, the periodicity and
25 impedance mismatch between the DE phases is tuned, which in turn change the Bragg reflections
26 and the desired band gaps (Shmuel & Band, 2016; Lustig & Shmuel, 2018).

27 To achieve a significant tunability, aforementioned works have shown that large electric fields
28 are needed—a requirement that hinders the practical utility of DEs as tunable phononic crystals.
29 Since this tunability is a function of the microstructure of the composite, Bortot et al. (2018)
30 have developed a scheme to identify unit cells that exhibit better performance based on *topology*
31 *optimization*—a numerical method that systematically searches for optimal material distribution
32 that under specified design and response constraints. As explained in more detail later, here we
33 go beyond this meta-heuristic optimization approach, by developing a gradient-based optimization
34 scheme for the problem considered by Bortot et al. (2018), building upon the model, governing
35 equations and analysis by Shmuel (2013).

36 Research on topology optimization began with the seminal paper of Bendsøe & Kikuchi (1988)
37 and recent advancements are discussed in several review articles (Sigmund & Maute, 2013; Deaton
38 & Grandhi, 2014). For computational implementation, the design domain—a square unit cell in
39 the current context—is discretized into a finite number of squares and a design variable is attached
40 to each of their centroids. The value of the design variable then indicates which material is placed
41 at the corresponding position in space. This allows for significant design freedom as there is no
42 assumption regarding the topology of the unit cell. Consequently, vast improvement in performance
43 can be achieved in comparison to unit cells of prescribed topology, e.g. a circular fiber within a
44 surrounding matrix.

45 The use of topology optimization for maximizing phononic band gaps was pioneered by Sigmund
46 & Søndergaard Jensen (2003). Their work was followed by many studies employing optimization
47 techniques for synthesizing phononic crystals such that desired band gap characteristics are obtained
48 (Halkjær & Jensen, 2006; Gazonas et al., 2006; Hussein et al., 2007; Bilal & Hussein, 2011; Liu
49 et al., 2014, 2016a; Li et al., 2016a; Liu et al., 2016b; Xie et al., 2017; Lu et al., 2017; Xie et al.,
50 2017; Chen et al., 2018; Yi et al., 2019; Liu et al., 2020; Quinteros et al., 2021; Zhang et al.,
51 2021). Detailed reviews on topology optimization of phononic crystals were provided by Yi &
52 Youn (2016) and Li et al. (2019).

53 The studies mentioned above aimed at optimizing the linear elastic response, while optimization
54 techniques have been employed only recently for band gaps that depend on nonlinear elastic deformations
55 (Hedayatrasa et al., 2016; Bortot et al., 2018; De Pascalis et al., 2020).

56 The limitation of these three studies, from the optimal design point of view, is that they are based
57 on metaheuristics, specifically Genetic Algorithms (GA). These methods utilize only function
58 evaluations and no gradient information is used to progress towards an optimum. Their main
59 drawback is that the number of function evaluations that is needed increases exponentially with
60 the number of design variables. Each evaluation consists of solving many generalized eigenvalue
61 problems for generating the band diagram. This computational bottleneck limits the design resolution,
62 i.e., the number of design variables that represent the material distribution, as can be seen in the
63 respective results (Hedayatrasa et al., 2016; Bortot et al., 2018; De Pascalis et al., 2020).

64 The full potential of topology optimization can only be accessed if gradient-based optimization
65 is used, so that the computational effort can be reduced by orders of magnitude and fine design
66 resolution can be accommodated. Such efficient approach is developed here for the case study
67 analyzed by Shmuel (2013), to which Bortot et al. (2018) applied GA optimization. The medium
68 that they analyzed comprises soft dielectric fibers embedded periodically in a matrix made of a
69 different deformable dielectric. The composite is quasistatically actuated by application of axial
70 electric field. Under the assumption of incompressible phases, Shmuel (2013) has found a closed-
71 form solution for the resultant deformation in terms of the bias electric field and the properties
72 of the composite. Using a plane-wave expansion approach, Shmuel (2013) determined the band
73 structure of incremental anti-plane waves propagating in the deformed configuration, the gaps of
74 which were optimized by Bortot et al. (2018) using a GA method.

75 Here, we introduce a finite element formulation of the incremental problem, and use the properties
76 of each element as the design variables, the objective of which is to maximize the width of the gap in
77 the audible frequency range. In order to iteratively update the design variables, we employ gradient-
78 based optimization, namely the Method of Moving Asymptotes—MMA (Svanberg, 1987). We
79 carry out and implement fully analytical sensitivity analysis for computing the gradient of the
80 objective function with respect to each one of the design variables. We generate optimized designs
81 with superior performance compared to those obtained by Bortot et al. (2018), while the computational
82 cost—in terms of the number of function evaluations—is smaller by orders of magnitude.

83 Before we proceed with details on the structure of this paper, it is important to note that the
84 constitutive model upon which we develop our equations neglects viscosity (Destrade & Saccomandi,
85 2004; Hong, 2011; Chiang Foo et al., 2012), to establish a starting point for gradient-based optimization
86 in a simpler setting. While our assumption is reasonable for silicon, it is not appropriate for
87 acrylics (Kornbluh & Pelrine, 2008), there viscosity is much more pronounced, and future work
88 will require the integration of viscoelastic theory into (see, e.g., the way in which Mohajer et al.
89 (2021) extended the work of Shmuel et al. (2012)). We also emphasize that the dynamic problem
90 considered here focuses exclusively on the anti-plane motion, i.e., assumes that the more complicated
91 in-plane motion is not excited. This assumption significantly simplifies the analysis; a more
92 complete investigation, which allows motions, is left for future work, and would require the framework
93 of Getz et al. (2017).

94 The paper is organized as follows. In Sec. 2 we provide the governing equations of electroelastic
95 composites (Dorfmann & Ogden, 2005; Suo et al., 2008; Gei et al., 2013; DeBotton et al., 2007;
96 Dorfmann & Ogden, 2010), upon which the forthcoming analysis is based. In Sec. 3 we recall the
97 solution of Shmuel (2013) to the quasistatic deformation of the periodic DE composite owing to

98 axial electric fields, and the equations developed therein for the incremental problem of anti-plane
 99 shear waves. In Sec. 4, we present the finite element formulation for the solution of the incremental
 100 problem, and specifically for the calculation of the band diagram of the deformed DE composite.
 101 The contribution of this work is detailed in Sec. 5 and Sec. 6, where we present the analytical design
 102 sensitivity analysis for computing the gradient of the objective function with respect to each one
 103 of the design variables; implement the method using in-house MatLab code; and present numerical
 104 examples. We conclude this paper with a summary of our results in Sec. 7.

105 2. Governing equations

106 To provide a self-contained report, here we briefly summarize the governing equations pertaining
 107 to nonlinear electro-mechanical deformation of dielectric elastomers following the theory of nonlinear
 108 electroelasticity (Dorfmann & Ogden, 2005; Suo et al., 2008) and the associated linearized incremental
 109 theory (Dorfmann & Ogden, 2010).

110 2.1. Nonlinear electroelasticity theory

111 Consider an arbitrary deformable dielectric composite body $\mathcal{B}^m \cup \mathcal{B}^f = \mathcal{B}$ made up of two
 112 incompressible homogeneous dielectric phases \mathcal{B}^m and \mathcal{B}^f , and surrounded by vacuum. In the
 113 undeformed configuration, the dielectric composite occupies a region $\mathcal{B}_0^m \cup \mathcal{B}_0^f = \mathcal{B}_0$ with the
 114 boundary $\partial\mathcal{B}_0$. An arbitrary material particle in this configuration is denoted by its position vector
 115 \mathbf{X} . When subjected to electromechanical loadings, the dielectric composite body is deformed and
 116 occupies a region $\mathcal{B}_t^m \cup \mathcal{B}_t^f = \mathcal{B}_t$ with boundary $\partial\mathcal{B}_t$. The position of a material particle in the
 117 deformed configuration is denoted by \mathbf{x} , which is related to \mathbf{X} through the nonlinear deformation
 118 map $\mathbf{x} = \chi(\mathbf{X}, t)$. The components of deformation gradient are given by $F_{iJ} = \frac{\partial \chi_i(\mathbf{X}, t)}{\partial X_J}$. The
 119 determinant of the deformation gradient relates the volume ratio of an infinitesimal element in the
 120 deformed state, dv , and its counterpart in the undeformed state, dV , such that $J = \det(\mathbf{F}) > 0$.
 121 The components of the right Cauchy-green tensor are $C_{IJ} = F_{iI}F_{iJ}$.

For quasi-electrostatic processes, in the absence of free charges and currents, Gauss's law and Faraday's law are written as

$$122 \frac{\partial d_i}{\partial x_i} = 0, \quad \frac{\partial e_j}{\partial x_k} \epsilon_{ijk} = 0_i, \quad (1)$$

123 respectively, where \mathbf{d} and \mathbf{e} are the electric displacement and the electric field vectors in the
 124 deformed configuration, respectively; $\mathbf{0}$ represents the zero vector and ϵ represents the Levi-Civita
 125 symbol. In addition, the mechanical equilibrium equation in the deformed configuration, in the
 absence of mechanical body forces, is

$$126 \frac{\partial \sigma_{ij}}{\partial x_j} = 0_i, \quad (2)$$

127 where σ is the symmetric *total* Cauchy stress tensor consisting of both mechanical and electrical
 contributions.

128 In this paper, we consider infinite, periodic, dielectric composites, which possess internal, mechanical
 129 traction and free charge interfaces between the two dielectric phases m and f with jump boundary
 130 conditions

$$[[\sigma_{ij}]] n_j = 0_i, \quad [[d_i]] n_i = 0, \quad [[e_i]] n_j \epsilon_{ijk} = 0_k, \quad (3)$$

131 where $\llbracket \bullet \rrbracket = (\bullet)^m - (\bullet)^f$ represents the jump of quantities between the two phases, and \mathbf{n} represents
 132 the unit normal vector on the deformed interface and directed from phase m to phase f .

In Lagrangian description that uses \mathbf{X} as the independent variable, the *total* first Piola–Kirchhoff stress tensor is related to the *total* Cauchy stress tensor by $P_{iJ} = J\sigma_{ik}F_{kJ}^{-T}$ and satisfies the Lagrangian form of the equilibrium equation

$$\frac{\partial P_{iJ}}{\partial X_J} = 0_i, \quad (4)$$

in the undeformed configuration \mathcal{B}_0 . The Lagrangian electric displacement and electric field are given as $D_J = JF_{Ji}^{-1}d_i$ and $E_J = F_{iJ}e_i$, respectively. They satisfy the Lagrangian form of Gauss’s law and Faraday’s law

$$\frac{\partial D_J}{\partial X_J} = 0, \quad \frac{\partial E_J}{\partial X_K} \epsilon_{IJK} = 0_I, \quad (5)$$

133 respectively.

134 We consider non-dissipative materials for which the first Piola–Kirchhoff stress tensor \mathbf{P} and
 135 Lagrangian electric field \mathbf{E} are obtained constitutively in terms of the deformation gradient \mathbf{F}
 136 and Lagrangian electric displacement \mathbf{D} through an *augmented* energy density function $\psi(\mathbf{F}, \mathbf{D})$
 137 as (Dorfmann & Ogden, 2005)

$$P_{iJ} = \frac{\partial \psi}{\partial F_{iJ}} - p_0 F_{iJ}^{-T}, \quad E_J = \frac{\partial \psi}{\partial D_J}, \quad (6)$$

138 where p_0 is a Lagrange multiplier that accounts for the incompressibility constraint.

139 2.2. The linearized incremental theory

Following Dorfmann & Ogden (2010), we present the governing equations pertaining to the time dependent infinitesimal increment in both elastic and electric displacement fields $\dot{\mathbf{x}} = \dot{\chi}(\mathbf{X}, t)$, $\dot{\mathbf{D}}(\mathbf{X}, t)$, respectively, superimposed on the static deformed configuration characterized by the fields $\chi(\mathbf{X}, t)$ and $\mathbf{D}(\mathbf{X}, t)$. Henceforth, the infinitesimal incremental quantities are denoted with the superposed dot. The *push-forwards* of increments in the *total* first Piola–Kirchhoff stress, the Lagrangian electric displacement and the Lagrangian electric fields are

$$\Sigma_{ij} = \frac{1}{J} \dot{P}_{iK} F_{jK}, \quad \check{d}_i = \frac{1}{J} F_{iJ} \dot{D}_J, \quad \check{e}_i = F_{ji}^{-1} \dot{E}_j, \quad (7)$$

140 respectively, satisfying the incremental forms of Gauss’s, Faraday’s laws, and momentum balance
 141 equation,

$$\frac{\partial \check{d}_i}{\partial x_i} = 0, \quad \frac{\partial \check{e}_j}{\partial x_k} \epsilon_{ijk} = 0_i, \quad \frac{\partial \Sigma_{ij}}{\partial x_j} = \rho \frac{\partial^2 \dot{x}_i}{\partial t^2}, \quad (8)$$

142 respectively, where $\dot{\mathbf{x}}(\mathbf{x}, t) := \dot{\chi}(\mathbf{X}, t)$.

143 For an incompressible dielectric elastomer material, the linearized incremental constitutive laws
 144 in terms of the increments Σ and \check{e} are obtained using Eq. (6) and the push-forward operation as

$$\begin{aligned} \Sigma_{ij} &= \mathcal{C}_{ijkl} h_{kl} + p_0 h_{ji} - \dot{p}_0 \delta_{ij} + \mathcal{B}_{ijk} \check{d}_k, \\ \check{e}_i &= \mathcal{B}_{lki} \dot{h}_{kl} + \mathcal{A}_{ij} \check{d}_j, \end{aligned} \quad (9)$$

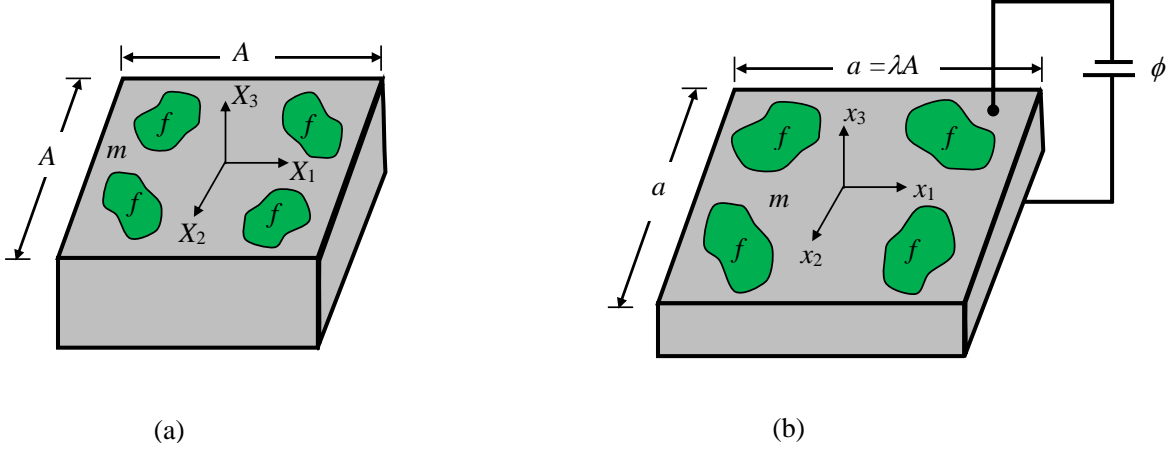


Figure 1: Dielectric elastomer fiber composite in the (a) undeformed configuration, and (b) deformed configuration, when subjected to an axial electric field.

where

$$\begin{aligned} \mathcal{C}_{ijkl} &= \frac{1}{J} F_{jI} \frac{\partial^2 \psi}{\partial F_{iJ} \partial F_{kL}} F_{lJ}, & \mathcal{B}_{ijk} &= F_{jI} \frac{\partial^2 \psi}{\partial F_{iI} \partial D_J} F_{Jk}^{-1}, \\ \mathcal{A}_{ij} &= J F_{Ii}^{-1} \frac{\partial^2 \psi}{\partial D_I \partial D_J} F_{Jj}^{-1}, \end{aligned} \quad (10)$$

145 are the spatial constitutive tangent moduli, and $h_{ij} = \frac{\partial \dot{x}_i}{\partial x_j}$ is subjected to incompressibility constraint

146 $h_{kk} = 0$.

147 3. Quasistatic finite deformation and incremental anti-plane shear waves in DE composites

148 As mentioned, using the above theory, Shmuel (2013) determined the quasistatic deformation of
 149 the periodic DE composite owing to axial electric fields [see also the study by Sharma et al. (2021)],
 150 and developed the equations that govern incremental anti-plane shear waves propagating through
 151 the deformed composite. In order to provide a self-contained report, we concisely recapitulate the
 152 quasistatic solution and incremental equations, to which we will employ a finite element solution
 153 and develop the optimization process.

154 We consider a dielectric elastomer composite that is infinitely periodic in the (x_1, x_2) plane. The
 155 composite is made of incompressible DE fibers along the x_3 direction with arbitrary cross-section
 156 (phase f), that are embedded in a different incompressible DE matrix (phase m). The constitutive
 157 response of the phases is given by the augmented Gentian free energy density function (Zhao et al.,
 158 2007; Sharma, 2020):

$$\psi(F_{iJ}, D_P) = -\frac{\mu J_m}{2} \ln \left[1 - \frac{F_{iJ} F_{iJ} - 3}{J_m} \right] + \frac{1}{2\varepsilon} D_P F_{iP} F_{iQ} D_Q, \quad (11)$$

where ε is the dielectric permittivity, μ is the shear modulus of the dielectric elastomer, J_m is a dimensionless material parameter that accounts for the strain stiffening that arises from the limited extensibility of the elastomers. Figure 1a shows the schematic of a square DE composite unit cell

of length A in the undeformed configuration. The composite is subjected to an average electric field of magnitude e_3 in the x_3 direction, and is free to expand in the transverse (x_1, x_2) plane. From an experimental viewpoint, such actuation is achieved by the application of a voltage drop between two compliant coated electrodes on the top and bottom faces of the composite, located far enough one of each other to avoid edge effects. Shmuel (2013) has shown that the resultant deformation and electric field are homogeneous, in the form

$$\mathbf{F}^{(m)} = \mathbf{F}^{(f)} = \begin{bmatrix} \lambda & 0 & 0 \\ 0 & \lambda & 0 \\ 0 & 0 & \lambda^{-2} \end{bmatrix}, \quad \mathbf{e}^{(m)} = \mathbf{e}^{(f)} = \begin{bmatrix} 0 \\ 0 \\ e_3 \end{bmatrix}, \quad (12)$$

159 where the in-plane stretch ratio λ is given by the solution of the nonlinear equation

$$\bar{\mu} (\lambda^2 - \lambda^{-4}) = \bar{\varepsilon} e_3^2, \quad (13)$$

160 where $\check{\mu}^{(p)} = \frac{\mu^{(p)} J_m^{(p)}}{J_m^{(p)} - 2\lambda^2 - \lambda^{-4} + 3}$, $(\bar{\bullet}) = v^{(m)}(\bullet) + v^{(f)}(\bullet)$ and $v^{(p)}$ is the volume fraction of
 161 phase p . Thus, up to the point of bifurcation, for any given value of applied electric field e_3 and
 162 properties of the composite, the solution of Eq. (13) delivers the resultant deformation.

163 On the top of deformed configuration, we consider anti-plane waves propagating in the (x_1, x_2)
 164 plane of the composite. The size of the composite in this plane is assumed large enough to be
 165 analyzed as an infinite periodic medium. Figure 2a shows the schematic of the DE fiber composite
 166 unit cell in the deformed (x_1, x_2) plane. Let $\dot{x}_3(\mathbf{x}, t)$ and $\dot{\phi}(\mathbf{x}, t)$ denote the anti-plane incremental
 167 displacement and the incremental electric potential, respectively; the equations that govern these
 168 two unknown fields are

$$\frac{\partial}{\partial x_j} \left(\tilde{\mu}(\mathbf{x}) \frac{\partial \dot{x}_3(\mathbf{x}, t)}{\partial x_j} - \tilde{d}(\mathbf{x}) \frac{\partial \dot{\phi}(\mathbf{x}, t)}{\partial x_j} \right) = \rho(\mathbf{x}) \frac{\partial^2 \dot{x}_3}{\partial t^2}, \quad (14)$$

$$\frac{\partial}{\partial x_j} \left(-\tilde{d}(\mathbf{x}) \frac{\partial \dot{x}_3(\mathbf{x}, t)}{\partial x_j} - \varepsilon(\mathbf{x}) \frac{\partial \dot{\phi}(\mathbf{x}, t)}{\partial x_j} \right) = 0, \quad (15)$$

169 respectively, where $j = 1, 2$, $\tilde{\mu}(\mathbf{x}) = \check{\mu}(\mathbf{x})\lambda^2 - \varepsilon(\mathbf{x})e_3^2$, and $\tilde{d}(\mathbf{x}) = \varepsilon(\mathbf{x})e_3$.

170 Eqs. (14)-(15) are the starting point of our analysis: in the next Sec. we develop a finite element
 171 formulation to solve them, and in turn obtain the band diagram of incremental anti-plane shear
 172 waves in the DE composite. Later on, based on the finite element formulation, we will develop a
 173 gradient-based topology optimization method, the objective of which is to identify optimal unit-
 174 cells that generate the widest band gaps at designated electric fields.

175 4. Finite element formulation

176 We introduce next a finite element formulation with Bloch-Floquet periodic boundary conditions
 177 (Kittel et al., 1996) to solve Eqs. (14)-(15). With $\delta \dot{x}_3$ and $\delta \dot{\phi}$ denoting virtual incremental anti-plane
 178 displacement and virtual incremental electric potential, respectively, the weak form statements

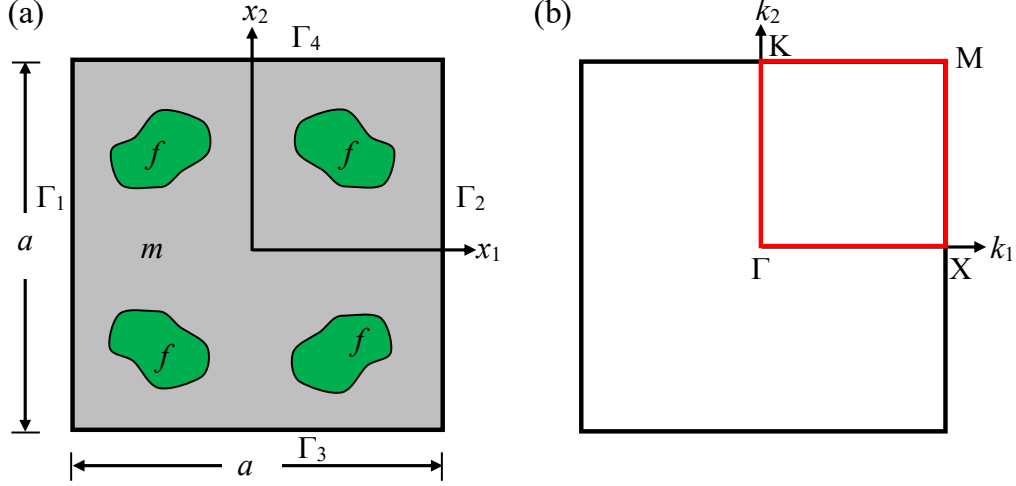


Figure 2: (a) Schematic description of the twice-symmetric square unit cell in the periodicity plane (x_1, x_2) , and (b) the corresponding first Brillouin zone with line segments to be scanned for determining the gaps extrema.

179 corresponding to Eq. (14) and Eq. (15) are written as

$$\int_{\mathcal{B}_t} \left(\tilde{\mu} \frac{\partial \dot{x}_3}{\partial x_j} - \tilde{d} \frac{\partial \dot{\phi}}{\partial x_j} \right) \frac{\partial \delta \dot{x}_3}{\partial x_j} ds = \int_{\mathcal{B}_t} \rho \delta \dot{x}_3 \frac{\partial^2 \dot{x}_3}{\partial t^2} ds, \quad (16)$$

$$\int_{\mathcal{B}_t} \left(-\tilde{d} \frac{\partial \dot{x}_3}{\partial x_j} - \varepsilon \frac{\partial \dot{\phi}}{\partial x_j} \right) \frac{\partial \delta \dot{\phi}}{\partial x_j} ds = 0, \quad (17)$$

180 respectively, where s is the area of the unit cell in the deformed configuration.

181 The DE composite unit cell is discretized using finite elements, $\mathcal{B}_t = \cup \mathcal{B}_t^e$, and finite element
 182 approximation for the incremental displacement and electric potential fields inside the element \mathcal{B}_t^e
 183 are written using the Voigt notation as

$$\dot{x}_3 = N_a \dot{x}_{a3}; \quad \dot{\phi} = N_a \dot{\phi}_a, \quad (18)$$

184 where N_a represents the shape function associated with node a of the element, and \dot{x}_{a3} and $\dot{\phi}_a$
 185 are the incremental anti-plane displacement and the incremental electric potential values at node
 186 a . Substituting above finite approximations and the linearized constitutive relations of Eq. (9) into
 187 Eqs. (16)-(17), the elemental level equations corresponding to momentum balance and Gauss law
 188 are written as

$$[K^{mm}] \{\dot{x}_{b3}\} + [K^{me}] \{\dot{\phi}_b\} = [M] \left\{ \frac{\partial^2 \dot{x}_{b3}}{\partial t^2} \right\}, \quad (19)$$

$$[K^{em}] \{\dot{x}_{b3}\} + [K^{ee}] \{\dot{\phi}_b\} = 0, \quad (20)$$

189 where K^{mm} is the mechanical stiffness matrix, K^{me} and K^{em} are the electro-mechanical coupled

190 stiffness matrices, K^{ee} is the electric stiffness matrix, and M is the mass matrix. The expressions
 191 for these elemental stiffness matrices are given as

$$K^{mm} = \int_{\mathcal{B}_t^e} \tilde{\mu} \frac{\partial N_a}{\partial x_j} \frac{\partial N_b}{\partial x_j} ds, \quad (21)$$

$$K^{me} = - \int_{\mathcal{B}_t^e} \tilde{d} \frac{\partial N_a}{\partial x_j} \frac{\partial N_b}{\partial x_j} ds, \quad (22)$$

$$K^{em} = - \int_{\mathcal{B}_t^e} \tilde{d} \frac{\partial N_a}{\partial x_j} \frac{\partial N_b}{\partial x_j} ds, \quad (23)$$

$$K^{ee} = - \int_{\mathcal{B}_t^e} \varepsilon \frac{\partial N_a}{\partial x_j} \frac{\partial N_b}{\partial x_j} ds, \quad (24)$$

$$M = \int_{\mathcal{B}_t^e} \rho N_a N_b ds. \quad (25)$$

192 Further, by assuming both the nodal incremental displacement and the incremental electric
 193 potential to be time harmonic as

$$\dot{x}_{b3} = \tilde{x}_b(x) e^{-i\omega t}; \quad \dot{\phi}_b = \tilde{\phi}_b(x) e^{-i\omega t}, \quad (26)$$

194 and inserting these harmonic expressions into Eqs. (19)-(20), we get the incremental elemental
 195 level equations governing the electro-elastic wave motion with angular frequency ω as

$$[K^{mm}] \{\tilde{x}_b\} + [K^{me}] \{\tilde{\phi}_b\} - \omega^2 [M] \{\tilde{x}_b\} = 0, \quad (27)$$

$$[K^{em}] \{\tilde{x}_b\} + [K^{ee}] \{\tilde{\phi}_b\} = 0, \quad (28)$$

196 where \tilde{x}_b and $\tilde{\phi}_b$ denote the spatially dependent nodal incremental displacement and electric potential
 197 fields, respectively. Eliminating $\tilde{\phi}_b$ from Eq. (27) by substituting $\{\tilde{\phi}_b\} = -[G][K^{em}]\{\tilde{x}_b\}$ from
 198 Eq. (28), we finally obtain the following eigenvalue problem

$$\begin{aligned} & ([K^{mm} - K^{me}GK^{em}] - \omega^2 [M]) \{\tilde{x}_b\} \\ & = ([K^*] - \omega^2 [M]) \{\tilde{x}_b\} = 0, \end{aligned} \quad (29)$$

199 where $K^* = K^{mm} - K^{me}GK^{em}$ and G denotes the Moore–Penrose pseudoinverse of the electric
 200 stiffness matrix K^{ee} .

201 Using the Bloch theorem (Kittel et al., 1996), we specify the periodic boundary conditions for
 202 analyzing the anti-plane wave propagation through the infinite, periodic DE composite. For the DE
 203 composite with square lattice shown in Fig. 2a, the Bloch periodic boundary conditions for the

204 nodal displacements are expressed as (Vatanabe et al., 2014; Jandron & Henann, 2018)

$$\begin{aligned}\tilde{x}_b(x_{\Gamma_2}) &= \exp(ik_1a)\tilde{x}_b(x_{\Gamma_1}), \\ \tilde{x}_b(x_{\Gamma_4}) &= \exp(ik_2a)\tilde{x}_b(x_{\Gamma_3}).\end{aligned}\quad (30)$$

205 Similarly, the Bloch periodic boundary conditions for the nodal electric potential fields are expressed
206 as

$$\begin{aligned}\tilde{\phi}_b(x_{\Gamma_2}) &= \exp(ik_1a)\tilde{\phi}_b(x_{\Gamma_1}), \\ \tilde{\phi}_b(x_{\Gamma_4}) &= \exp(ik_2a)\tilde{\phi}_b(x_{\Gamma_3}),\end{aligned}\quad (31)$$

207 where k_1 and k_2 are the component of real Bloch wave vector $\mathbf{k} = k_i e_i$ along x_1 and x_2 directions,
208 as shown in Fig. 2b. In order to implement these complex-valued boundary conditions, we used
209 the augmented penalty method (Felippa, 2001; Oliveira et al., 2010).

210 The eigenvalue problem stated in Eq. (29) along with the Bloch periodic boundary conditions
211 of Eqs. (30)-(31) is solved for computing the band diagram, i.e, ω as a function of the wave vector
212 \mathbf{k} . Due to the quarter symmetry of the problem considered in this paper (see Fig. 2a), it is sufficient
213 to consider only the wave vector along the edges $[\Gamma - X - M - K - \Gamma]$ of the first Brillouin
214 zone, marked by red lines in Fig. 2b (Sigmund & Søndergaard Jensen, 2003; Vatanabe et al., 2014;
215 Meng et al., 2017; Yi & Youn, 2016). The coordinates of various points along these edges are as
216 $\Gamma = (0, 0)$, $X = (\pi/a, 0)$, $M = (\pi/a, \pi/a)$, and $K = (0, \pi/a)$.

217 Having at hand a finite-element formulation to calculate the band diagram, we proceed next to
218 develop the gradient-based topology optimization method, whose aim is to find the microstructure
219 that results with the widest band gaps at prescribed electric fields.

220 5. Topology optimization

221 In the design of phononic band gap structures, we need to find the unit cell that yields the
222 desired band gap characteristics. In this section, we introduce the topology optimization method
223 for obtaining the optimized distribution of the matrix and fiber phases in the DE composite unit cell
224 that maximizes the band gap size.

225 5.1. Material property interpolation for topology optimization

226 In this work, the design domain is a unit cell that is discretized by finite elements. To interpolate
227 the material properties for each finite element used to discretize the design domain, artificial design
228 variables $\xi^e \in [0, 1]$ ($e = 1, 2, \dots, N$, N being the total number of finite elements in the design
229 domain) are assigned to all finite elements as shown in Fig. 3.

230 For example, $\xi^e = 0$ represents an element e that is composed of matrix phase, while $\xi^e = 1$
231 represents an element consisting of fiber phase. As discussed by Sigmund & Søndergaard Jensen
232 (2003) and Meng et al. (2017), the material properties for each finite element in the design domain
233 can be interpolated linearly between the matrix and fiber phases as

$$\rho^e = (1 - \xi^e)\rho^{(m)} + \xi^e\rho^{(f)}, \quad (32)$$

$$\mu^e = (1 - \xi^e)\mu^{(m)} + \xi^e\mu^{(f)}, \quad (33)$$

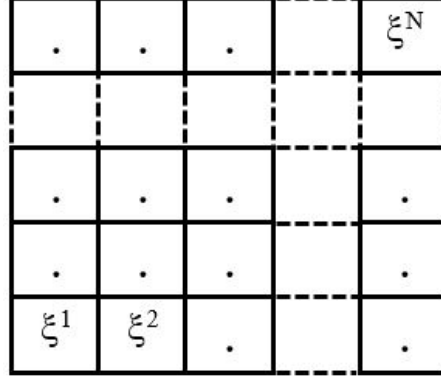


Figure 3: Discretization of the unit cell into N finite elements and assignment of a design variable to each finite element.

$$\varepsilon^e = (1 - \xi^e)\varepsilon^{(m)} + \xi^e\varepsilon^{(f)}, \quad (34)$$

$$J_m^e = (1 - \xi^e)J_m^{(m)} + \xi^e J_m^{(f)}. \quad (35)$$

234 5.2. Optimization problem

The topology optimization problem aims to maximize the band gap width between the two adjacent bands in the audible frequency range 0-10 kHz. For two adjacent bands, assuming the eigenfrequencies corresponding to overlying band and underlying band to be ω_{j+1} and ω_j , respectively, the objective function may be written as

$$f = \begin{cases} 10\text{kHz} - \max \omega_j(\xi, \mathbf{k})/2\pi \\ \quad \text{if } \min \omega_{j+1}(\xi, \mathbf{k})/2\pi \geq 10\text{kHz}, \\ (\min \omega_{j+1}(\xi, \mathbf{k}) - \max \omega_j(\xi, \mathbf{k}))/2\pi \\ \quad \text{if } \min \omega_{j+1}(\xi, \mathbf{k})/2\pi \leq 10\text{kHz}, \end{cases} \quad (36)$$

235 where, $\max \omega_j(\xi, \mathbf{k})$ and $\min \omega_j(\xi, \mathbf{k})$ represent the maximum and minimum of the j^{th} eigenfrequency
 236 ω_j , respectively, over the \mathbf{k} vector for a given design of the unit cell domain, ξ .

237 We note that this objective function is not strictly differentiable because the location of maximum
 238 and minimum eigenvalues over the \mathbf{k} -vector may change from one design iteration to another. The
 239 problem can be regularized using smooth maximum and minimum functions, as described in the
 240 appendix. The results we achieved with the smooth formulation are essentially identical to those
 241 achieved with the objective of Eq. (36) and therefore we limit the discussion to a brief comparison
 242 in the appendix. It should be noted that in most gradient-based topology optimization studies on
 243 band gaps, the issue of differentiability is not discussed and we presume that the results reported
 244 in the literature were obtained with standard maximum and minimum operators. One exception we
 245 found is the work of Qian & Sigmund (2011) where a smooth bound formulation is employed.

246

The topology optimization problem may be stated as

$$\begin{aligned} & \max_{\xi} \quad f \\ & \text{s.t. :} \quad (K^*(\mathbf{k}) - \omega^2 M) \tilde{x}_b = 0, \quad \mathbf{k} \in [\Gamma - X - M - K - \Gamma] \\ & \quad \quad 0 \leq \xi_e \leq 1, \quad e = 1, \dots, N. \end{aligned} \quad (37)$$

247 5.3. Design sensitivity analysis

248 In order to iteratively update the design variables, we utilize gradient-based optimization, specifically
249 MMA (Svanberg, 1987). This requires the evaluation of the gradient of the objective function with
250 respect to any individual design variable, ξ^e . The derivative of the objective function f in Eq. (36)
251 with respect to the design variable ξ^e is obtained as

$$\frac{\partial f}{\partial \xi^e} = \begin{cases} -\frac{1}{2\pi} \frac{\partial (\max \omega_n(\xi, \mathbf{k}))}{\partial \xi^e}, & \text{if } \min \omega_{n+1}(\xi, \mathbf{k})/2\pi \geq 10\text{kHz}; \\ \frac{1}{2\pi} \left(\frac{\partial (\min \omega_{n+1}(\xi, \mathbf{k}))}{\partial \xi^e} - \frac{\partial (\max \omega_n(\xi, \mathbf{k}))}{\partial \xi^e} \right), & \text{if } \min \omega_{n+1}(\xi, \mathbf{k})/2\pi \leq 10\text{kHz}. \end{cases} \quad (38)$$

252 For evaluating the objective function derivative in Eq. (38), the derivative of the eigenfrequency
253 with respect to the design variable must be evaluated. For a given wave vector \mathbf{k} , the derivative of
254 an eigenfrequency ω_n with respect to the design variable is computed by differentiating Eq. (29)
255 with respect to the design variable ξ^e , as follows

$$\frac{\partial (\omega_n(\xi, \mathbf{k}))}{\partial \xi^e} = \frac{1}{2\omega_n} \tilde{x}_b^{*T} \left(\frac{\partial K^*(\mathbf{k})}{\partial \xi^e} - \omega_n^2 \frac{\partial M}{\partial \xi^e} \right) \tilde{x}_b^*, \quad (39)$$

256 where, \tilde{x}_b^* is the global mass normalized eigenvector, and the derivative of the condensed stiffness
257 matrix K^* with respect to the design variable is obtained as

$$\begin{aligned} \frac{\partial K^*}{\partial \xi^e} &= \frac{\partial K^{mm}}{\partial \xi^e} - \frac{\partial K^{me}}{\partial \xi^e} (K^{ee})^{-1} K^{em} + \\ & K^{me} (K^{ee})^{-2} K^{em} \frac{\partial K^{ee}}{\partial \xi^e} - K^{me} (K^{ee})^{-1} \frac{\partial K^{em}}{\partial \xi^e}. \end{aligned} \quad (40)$$

258 The derivatives of the stiffness and the mass matrices $\frac{\partial K^{mm}}{\partial \xi^e}$, $\frac{\partial K^{me}}{\partial \xi^e}$, $\frac{\partial K^{em}}{\partial \xi^e}$, $\frac{\partial K^{ee}}{\partial \xi^e}$, and $\frac{\partial M}{\partial \xi^e}$
259 in Eqs. (39)-(40), are evaluated using Eqs. (21)-(25) as follows

$$\frac{\partial K^{mm}}{\partial \xi^e} = \int_{\mathcal{B}_i^e} \frac{\partial \tilde{\mu}^e}{\partial \xi^e} \frac{\partial N_a}{\partial x_j} \frac{\partial N_b}{\partial x_j} ds, \quad (41)$$

$$\frac{\partial K^{me}}{\partial \xi^e} = - \int_{\mathcal{B}_i^e} \frac{\partial \tilde{d}^e}{\partial \xi^e} \frac{\partial N_a}{\partial x_j} \frac{\partial N_b}{\partial x_j} ds, \quad (42)$$

$$\frac{\partial K^{em}}{\partial \xi^e} = - \int_{\mathcal{B}_i^e} \frac{\partial \tilde{d}^e}{\partial \xi^e} \frac{\partial N_a}{\partial x_j} \frac{\partial N_b}{\partial x_j} ds, \quad (43)$$

$$\frac{\partial K^{ee}}{\partial \xi^e} = - \int_{\mathcal{B}_i^e} \frac{\partial \varepsilon^e}{\partial \xi^e} \frac{\partial N_a}{\partial x_j} \frac{\partial N_b}{\partial x_j} ds, \quad (44)$$

$$\frac{\partial M}{\partial \xi^e} = \int_{\mathcal{B}_i^e} \frac{\partial \rho^e}{\partial \xi^e} N_a N_b ds, \quad (45)$$

260 in which the calculation of the derivatives of material parameters ρ^e , ε^e and \tilde{d}^e with regard to ξ_e is
 261 straightforward from Eqs. (32) and (34): $\frac{\partial \rho^e}{\partial \xi^e} = \rho^{(f)} - \rho^{(m)}$, $\frac{\partial \varepsilon^e}{\partial \xi^e} = \varepsilon^{(f)} - \varepsilon^{(m)}$, and $\frac{\partial \tilde{d}^e}{\partial \xi^e} = e_3 \frac{\partial \varepsilon^e}{\partial \xi^e}$,
 262 while the evaluation of the derivative of $\tilde{\mu}^e$ with regard to ξ_e is more involved, as follows ¹

$$\begin{aligned} \frac{\partial \tilde{\mu}^e}{\partial \xi^e} = & \frac{\left[2\mu^e J_m^e \lambda \frac{\partial \lambda}{\partial \xi^e} + \lambda^2 \left(\mu^e \frac{\partial J_m^e}{\partial \xi^e} + \frac{\partial \mu^e}{\partial \xi^e} J_m^e \right) \right]}{(J_m^e - 2\lambda^2 - \lambda^{-4} + 3)} \\ & - \frac{\mu^e J_m^e \lambda^2 \left[\frac{\partial J_m^e}{\partial \xi^e} - 4\lambda \frac{\partial \lambda}{\partial \xi^e} + 4\lambda^{-5} \frac{\partial \lambda}{\partial \xi^e} \right]}{(J_m^e - 2\lambda^2 - \lambda^{-4} + 3)^2} - \frac{\partial \varepsilon^e}{\partial \xi^e} e_3^2, \end{aligned} \quad (46)$$

263 where $\frac{\partial J_m^e}{\partial \xi^e} = J_m^{(f)} - J_m^{(m)}$, and the derivative of the stretch parameter with respect of design
 264 variable $\frac{\partial \lambda}{\partial \xi^e}$ is evaluated by differentiating Eq. (13) with respect to ξ^e and expressed as

$$\frac{\partial \lambda}{\partial \xi^e} = \frac{\left[(\varepsilon^{(f)} - \varepsilon^{(m)}) e_3^2 - (\lambda^2 - \lambda^{-4}) \left(\frac{\mu^e (J_m^{(f)} - J_m^{(m)}) + J_m^e (\mu^{(f)} - \mu^{(m)})}{(J_m^e - 2\lambda^2 - \lambda^{-4} + 3)} + \frac{\mu^e J_m^e (J_m^{(f)} - J_m^{(m)})}{(J_m^e - 2\lambda^2 - \lambda^{-4} + 3)^2} \right) \right]}{\left[(2\lambda^2 + 4\lambda^{-5}) \left(\sum_{e=1}^N \mu^e \right) + (\lambda^2 - \lambda^{-4}) (4\lambda - 4\lambda^{-5}) \left(\sum_{e=1}^N \frac{\mu^e J_m^e}{(J_m^e - 2\lambda^2 - \lambda^{-4} + 3)^2} \right) \right]}. \quad (47)$$

¹Note that the expression (46) corresponds to $\tilde{\mu}^e$ and ξ^e of the same finite element. However, in the evaluation of $\tilde{\mu}^e$ there exists a weak coupling to other elements due to the solution of λ that is a global state variable. Hence, for two distinct elements denoted e_1 and e_2 , the derivative is

$$\frac{\partial \tilde{\mu}^{e_1}}{\partial \xi^{e_2}} = \frac{2\mu^{e_1} J_m^{e_1} \lambda \frac{\partial \lambda}{\partial \xi^{e_2}}}{(J_m^{e_1} - 2\lambda^2 - \lambda^{-4} + 3)} - \frac{\mu^{e_1} J_m^{e_1} \lambda^2 \left[-4\lambda \frac{\partial \lambda}{\partial \xi^{e_2}} + 4\lambda^{-5} \frac{\partial \lambda}{\partial \xi^{e_2}} \right]}{(J_m^{e_1} - 2\lambda^2 - \lambda^{-4} + 3)^2}.$$

These coupling terms are several orders of magnitude smaller than the terms of (46) and were found to have no influence on the optimized design. Hence they are omitted from subsequent derivations.

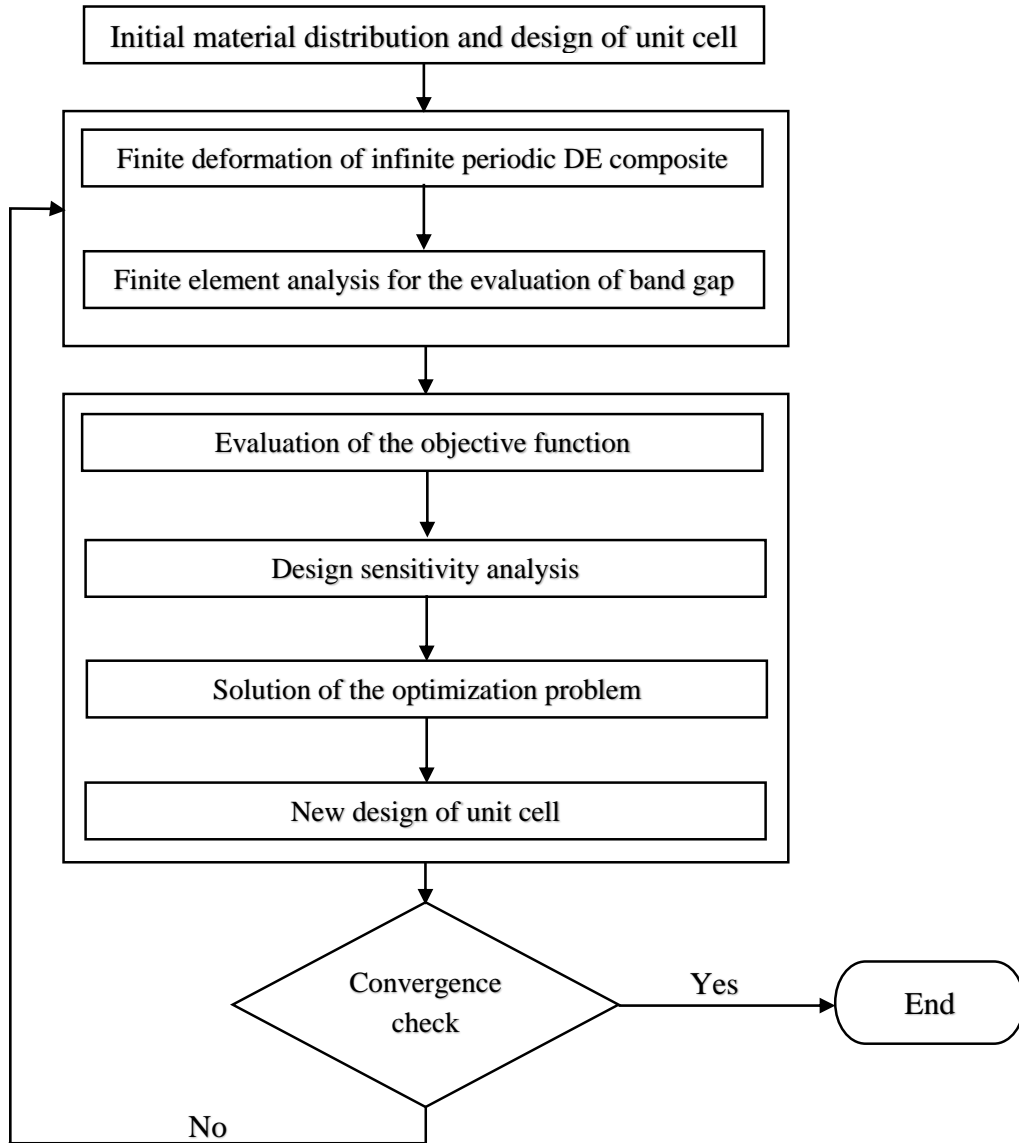


Figure 4: A schematic representation of the optimization process.

265 *5.4. Implementation*

266 The topology optimization framework presented in this paper is implemented by developing
 267 an in-house MATLAB code. The topology optimization process starts with generating one quarter
 268 of a twice-symmetric structure of the unit cell. In order to generate a symmetric unit cell, we
 269 randomly distribute design variables in one quarter of the unit cell, and assign these design variables
 270 symmetrically in the other three quarters. We note that this initial unit cell structure may not have
 271 gaps in its spectrum. Then, based on the finite element framework introduced in Section 3, we
 272 obtain the band diagram and the corresponding eigenvectors. Accordingly, the objective function
 273 is evaluated. Subsequently, we evaluate the gradient of the objective with respect to the design
 274 variables using Eq. (38). According to the evaluated objective function gradients, MMA proposes
 275 a new vector of design variables by solving a convex subproblem. This yields the formation of a

Table 1: Material properties.

	Material	
	Silicone CF19-2186	Polyurethane PT6100S
Shear modulus μ (kPa)	333	5667
Locking parameter J_m	46.3	6.67
Relative permittivity ϵ_r	2.8	7
Density ρ (kg/m ³)	1100	1200

276 new structure with the updated design variables. Thereafter, we repeat the finite element analysis
 277 for the evaluation of band gaps and MMA optimization scheme for updating the design variables.
 278 Such an iterative process continues until the maximum change in any design variable is less than
 279 10^{-6} . Figure 4 depicts schematic representation of the iterative optimization process.

280 6. Numerical results and discussions

281 In this section, we provide the numerical results for the phononic band gaps in dielectric
 282 elastomers designed by using the topology optimization framework presented in the previous section.
 283 The dielectric elastomer composite is assumed to be composed of polyurethane PT6100S fibers
 284 embedded in the silicone CF19-2186 matrix (Getz et al., 2017). The properties of these materials
 285 are listed in Table 1. In the undeformed configuration, we set the lattice parameter or the size of
 286 the square unit cell to be $A = 6.3$ mm. In order to discretize the unit cell, we used the four nodes,
 287 linear quadrilateral finite elements with two degrees of freedom (one anti-plane displacement and
 288 one electric potential) per node.

289 6.1. Validation of the finite element framework

290 First, for validating the finite element framework presented in Section 4 and investigating the
 291 influence of the bias electric field on the band structure, we compute the performance of a standard
 292 unit cell composed of circular fibers embedded in the matrix, as shown in Fig. 5a. The volume
 293 fraction of fibers in the unit cell is taken to be 0.5. The unit cell is discretized by 1139 quadrilateral
 294 finite elements as shown in Fig. 5a (left). In all the plots in this paper, the yellow color denotes the
 295 fiber and the blue color denotes the matrix. For investigating the effect of the bias electric field on
 296 the band diagram, we perform two cases, one without bias electric field ($e_3 = 0$) and the other with
 297 bias electric field $e_3 = 300$ MV/m. For both cases, without and with bias electric field, Figs. 5b and
 298 5c, respectively, compare the band structure computed using the finite element framework presented
 299 in this work and the plane wave expansion method (PWE) (Shmuel, 2013). The plot shows a very
 300 good agreement between FEM and PWE, validating our finite element framework. From the band
 301 diagrams, it is evident that the width of the widest gap at $e_3 = 0$, i.e., ($\Delta\omega/2\pi = 0.7626$ kHz), is
 302 smaller than that at $e_3 = 300$ MV/m, i.e., ($\Delta\omega/2\pi = 0.8073$ kHz), denoting an increase in the band
 303 gap width of 5.86%. This example suggests that the bias electric field has a favorable impact as it
 304 improves the maximization of band gap widths.

305 6.2. Topology optimization results

306 In this section, first, we present the topologies for the maximization of the band gap width
 307 between the first four adjacent bands (i.e., 1st and 2nd bands, 2nd and 3rd bands, 3rd and 4th bands,

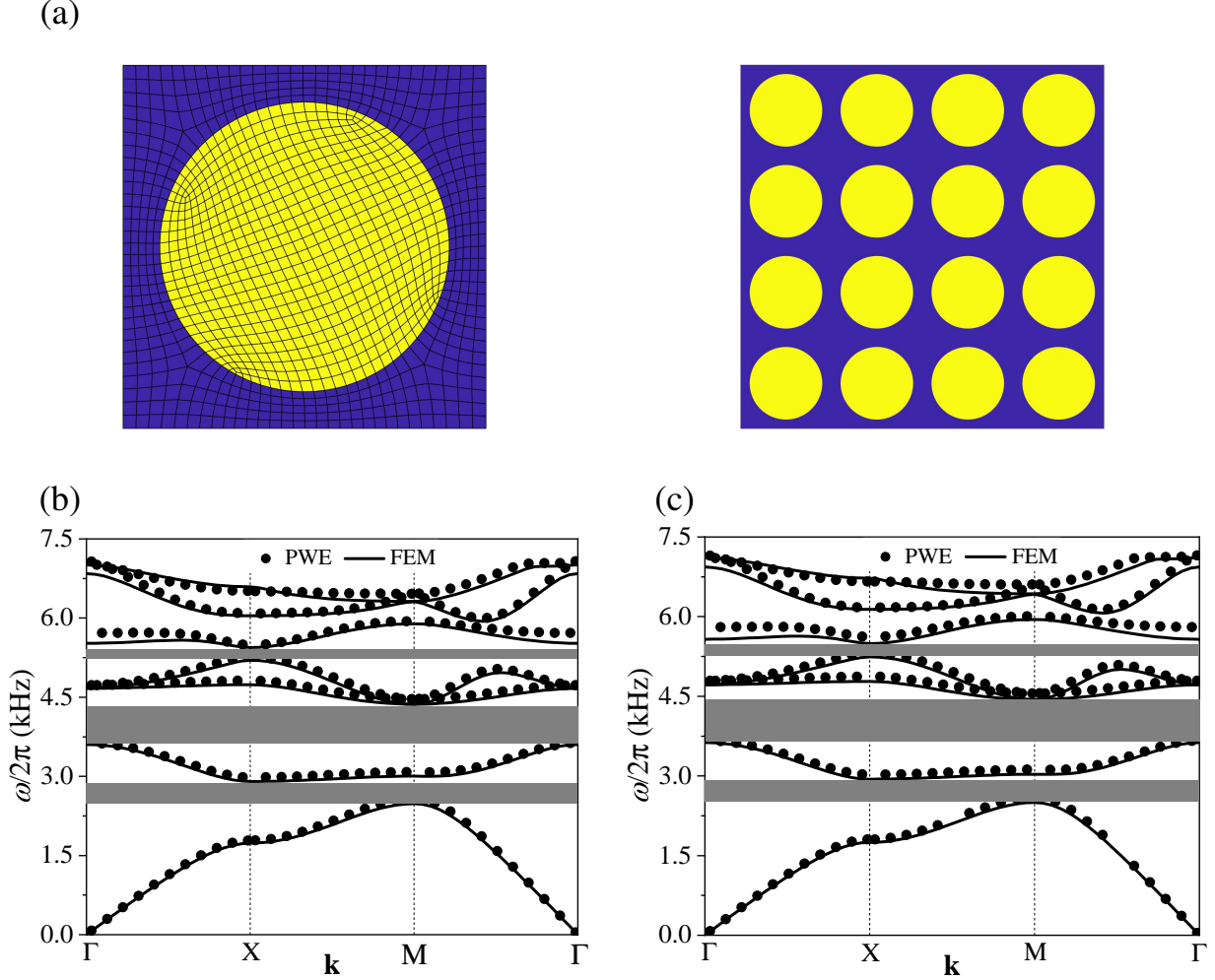


Figure 5: Influence of the bias electric field on the band structure of a DE composite with circular fiber and comparison of FEM results (solid lines) with the plane wave expansion method (PWE) results (symbols): (a) Unit cell (left) and periodic matrix (right), band diagrams (b) when bias electric field $e_3 = 0$, and (c) when bias electric field $e_3 = 300$ MV/m.

308 & 4th and 5th bands) and identify the two adjacent bands that have the largest optimized band gap
 309 in the audible frequency range. For these four optimization cases, we consider two values of the
 310 applied electric field, i.e., $e_3 = 150$ MV/m and $e_3 = 300$ MV/m, and discretize the unit cell by
 311 20×20 , bi-linear quadrilateral elements. The initial material distribution of the unit cells is taken
 312 to be random. The resulting designs of the unit cells that optimize the band gap widths between
 313 the first four adjacent bands at applied electric field $e_3 = 150$ MV/m and $e_3 = 300$ MV/m are
 314 depicted in the left panels of Figs. 6 and 7, respectively. In both figures, the middle panels represent
 315 the periodic matrices composed of four optimized unit cells, while the right panels show the band
 316 diagrams corresponding to the optimized unit cells depicted in the left panels. The estimates of
 317 the optimized band gaps between the first four adjacent bands and the corresponding fiber volume
 318 fractions for both the applied electric field values are listed in Table 2. From Table 2 and the left
 319 panels of Figs. 6 and 7, we observe the maximum band gap width when the band gap is optimized
 320 between the 4th and 5th bands. At $e_3 = 150$ MV/m, the value of the maximal band gap width in

Table 2: Optimized band gaps and fiber volume fractions, when maximizing gaps between two different adjacent bands.

Bias electric field (e_3) \rightarrow	150 MV/m		300 MV/m	
	Band gap	Fiber fraction	Band gap	Fiber fraction
1 st and 2 nd bands	1.58	0.65	1.71	0.66
2 nd and 3 rd bands	1.94	0.58	2.25	0.57
3 rd and 4 th bands	1.73	0.57	2.08	0.58
4 th and 5 th bands	4.31	0.67	4.61	0.68

321 the audible frequency range is 4.31kHz and the corresponding fiber volume fraction is 0.67. The
 322 maximal band gap width achieved in the audible frequency range at $e_3 = 300$ MV/m, is 4.61kHz
 323 with 0.68 fiber volume fraction.

324 Next, for the identified adjacent bands (i.e., 4th and 5th bands) representing maximum optimized
 325 band gap in the audible frequency range, we present the optimized designs for different initial
 326 layouts of the unit cells. We consider three initial layouts of the unit cells (fully random, single
 327 central square fiber inclusion, and fiber inclusions at multiple locations) as shown in Table 3. For
 328 these three initial layouts, the iteration history of the objective function and the evolution of the
 329 optimal topology of the unit cells at applied electric fields $e_3 = 150$ MV/m and $e_3 = 300$ MV/m
 330 are represented in Figs. 8 and 9, respectively. In both figures, the left columns show the iteration
 331 history of the objective function and the evolution of the unit cell structure for a random initial
 332 material distribution; the middle columns show the same data for an initial design consisting of
 333 a central square fiber inclusion; and the right columns show the same data for an initial design
 334 with fiber inclusions at multiple locations. From Figs. 8 and 9, we observe that the optimized
 335 topologies depend on the initial layouts. This phenomenon of dependency on the initial layouts for
 336 the unconstrained band gap maximization problem has been previously described in the literature
 337 (Yi et al., 2019; Li et al., 2016b) and is somewhat expected in gradient-based optimization. From
 338 the plots of the iteration histories of the objective function, we observe that the objective function
 339 increases rapidly at the starting stage of the topology optimization process and then the convergence
 340 rate becomes significantly slowed down over the iterations. The estimates of the optimized band
 341 gaps and the corresponding fiber volume fractions for all three initial layouts and both the values of
 342 the applied electric field are listed in Table 3. As evident from Table 3, the third initial guess (fiber
 343 inclusions at multiple locations) for the unit cell layout is best among all the three initial guesses,
 344 as it shows the maximum optimized band gap for both values of the applied electric fields. The
 345 maximum band gap achieved at $e_3 = 150$ MV/m is 4.37 kHz and that at $e_3 = 300$ MV/m is
 346 equal to 4.61 kHz. The fiber volume fractions corresponding to optimized layouts are the same for
 347 both applied electric field and are equal to 0.68. As evident from the convergence history plots,
 348 for the third initial layout of the unit cell, the topology optimization process converges faster in
 349 comparison to the other two initial layouts. This is expected because it utilizes an educated initial
 350 guess.

351 Next, we investigate the dependence of the optimized band gaps and the unit cell designs
 352 on the FE mesh resolution, that affects the design resolution. For this purpose, we study the
 353 maximization of band gap width between the 4th and 5th bands (i.e., having the highest band gaps in
 354 the audible frequency range). For mesh dependency analyses, we discretize the unit cell by 20×20 ,

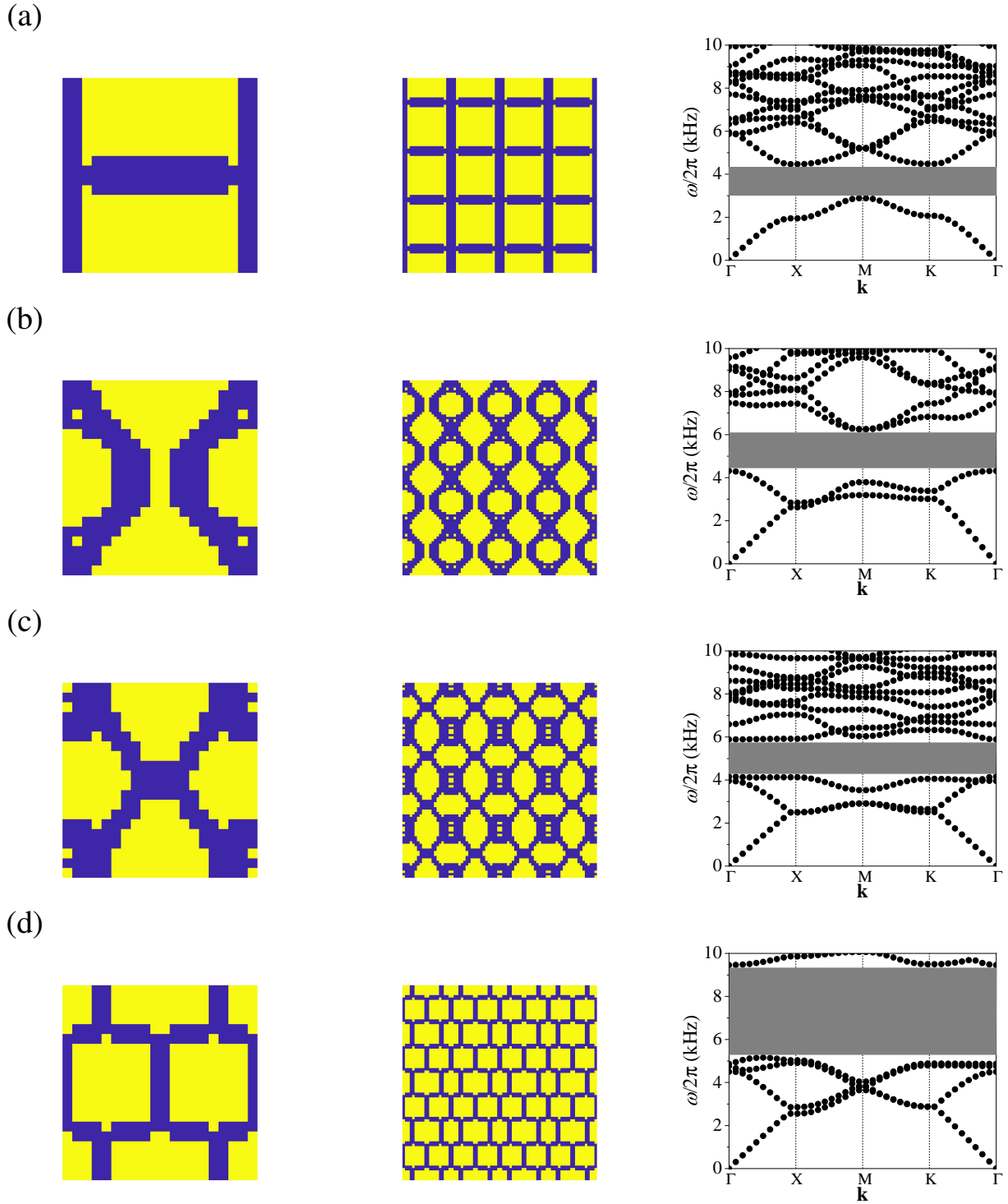


Figure 6: Unit cells (left), periodic matrices composed of 4×4 unit cells (middle), and band diagrams (right) of the optimized results when maximizing the band gap between (a) 1st and 2nd bands, (b) 2nd and 3rd bands, (c) 3rd and 4th bands, and (d) 4th and 5th bands, when bias electric field $e_3 = 150$ MV/m.

355 30×30 , and 40×40 bi-linear square finite elements, and perform the topology optimizations for
 356 maximizing the band gaps at the aforementioned two values of the applied electric field. For all

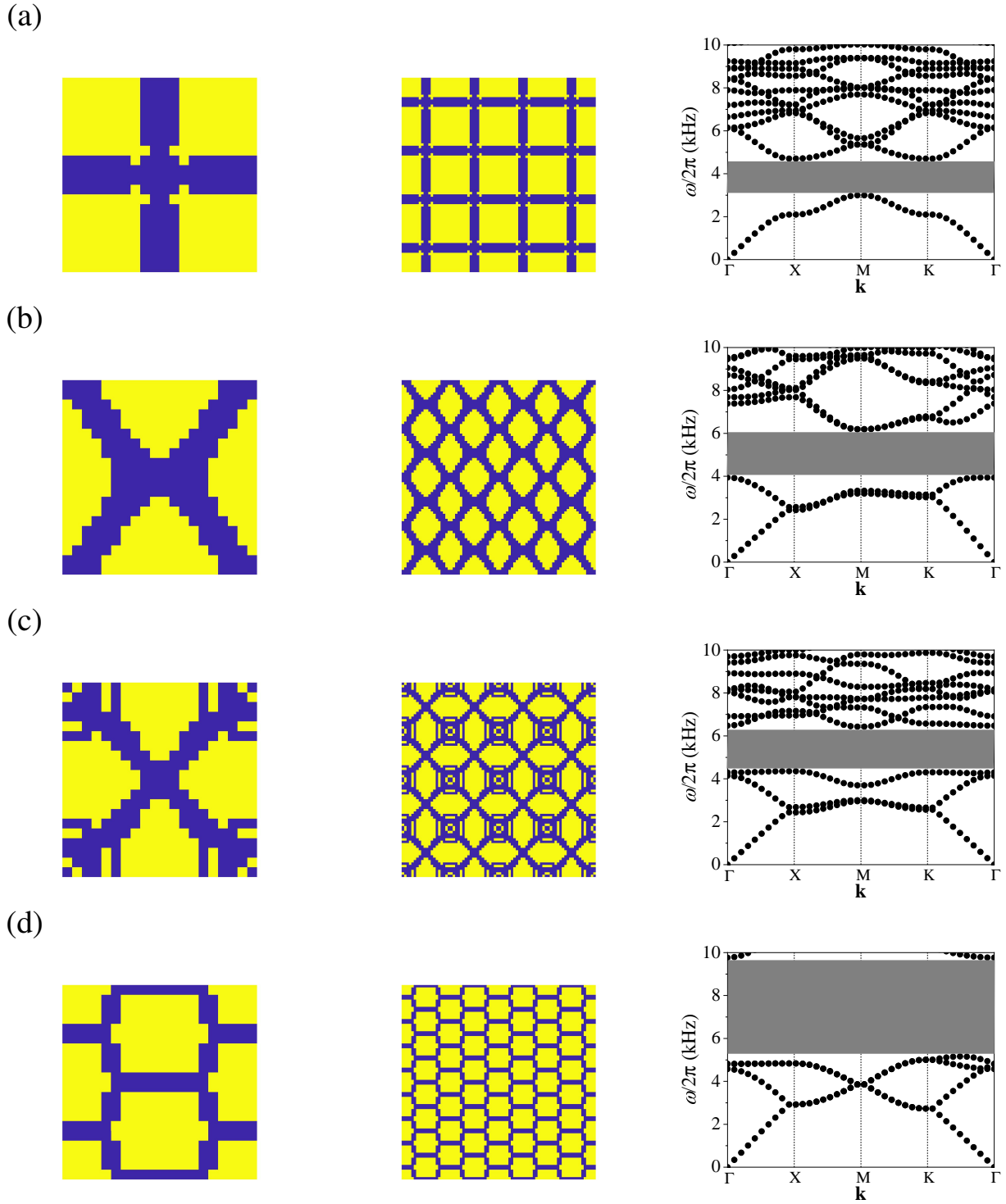


Figure 7: Unit cells (left), periodic matrices composed of 4×4 unit cells (middle), and band diagrams (right) of the optimized results when maximizing the band gap between (a) 1st and 2nd bands, (b) 2nd and 3rd bands, (c) 3rd and 4th bands, and (d) 4th and 5th bands, when bias electric field $e_3 = 300$ MV/m.

357 three mesh densities, we consider the same initial layout of the unit cell, i.e., the third layout of the
 358 aforementioned discussion for which we obtained the maximum at both the applied electric fields.

Table 3: Effect of initial material layout on the optimized band gaps and fiber volume fractions for maximization of band gap between 4th and 5th bands.

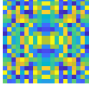


Initial material layout →						
Bias electric field (e_3)	Band gap	Fiber fraction	Band gap	Fiber fraction	Band gap	Fiber fraction
150 MV/m	4.31 kHz	0.67	4.30 kHz	0.68	4.37 kHz	0.68
300 MV/m	4.61 kHz	0.68	4.51 kHz	0.68	4.61 kHz	0.68

Table 4: Effect of mesh size on the optimized band gaps and fiber volume fractions for maximization of band gap between 4th and 5th bands.

Mesh density →	20×20		30×30		40×40	
Bias electric field (e_3)	Band gap	Fiber fraction	Band gap	Fiber fraction	Band gap	Fiber fraction
150 MV/m	4.37 kHz	0.680	4.33 kHz	0.715	4.30 kHz	0.680
300 MV/m	4.61 kHz	0.680	4.56 kHz	0.706	4.53 kHz	0.680

359 The optimized designs of the unit cell and the corresponding band diagrams for 20×20, 30×30,
360 and 40×40 mesh densities and at $e_3 = 150$ MV/m are compared in the left, middle and right panels
361 of Fig. 10a, respectively. For both values of bias electric field, the estimates of the optimized band
362 gaps and the corresponding fiber volume fractions at the aforementioned three mesh densities are
363 listed in Table 4. From the table, it is evident that the value of the optimized band gap decreases
364 with an increase in the mesh density for both the values of the bias electric field. This is attributed
365 to the effect of FE mesh refinement on the evaluation of the band gap. Interestingly, at 20×20 and
366 40×40 mesh density, we obtain the same designs of the unit cell and fiber volume fractions for both
367 values of the applied electric field.

368 Further, for a one-to-one comparison of the optimized unit cell structures obtained at different
369 mesh sizes, we evaluate the band gaps for all three optimized structures on a 120×120 mesh
370 resolution. This resolution is chosen such that all optimized designs can be projected precisely
371 to a common mesh. Table 5 enlists the band gap values evaluated on a 120×120 mesh resolution
372 for the optimized unit cells obtained at the aforementioned three mesh densities and two values
373 of bias electric field. The band diagrams evaluated at 120×120 mesh resolution of the unit cells
374 optimized at three mesh sizes are shown in Fig. 11. From Table 5, we can see that as the design
375 resolution increases, so does the width of the optimized band gap. This demonstrates the efficacy
376 of the topology optimization method: better performance can be achieved by increasing the design
377 resolution, hence expanding the design space. The unit cell layouts obtained from the optimization
378 at 40×40 mesh density show the maximum band gap for both bias electric fields. For 120×120
379 mesh resolution, the value of maximum band gap achieved at $e_3 = 150$ MV/m is 4.24 kHz with
380 0.68 fiber volume fraction and that at $e_3 = 300$ MV/m is equal to 4.44 kHz with the same fiber
381 volume fraction of 0.68.

382 Finally, we discuss the advantages of the gradient-based topology optimization framework
383 developed in this paper over the method based on PWE and a genetic algorithm (GA) for maximization

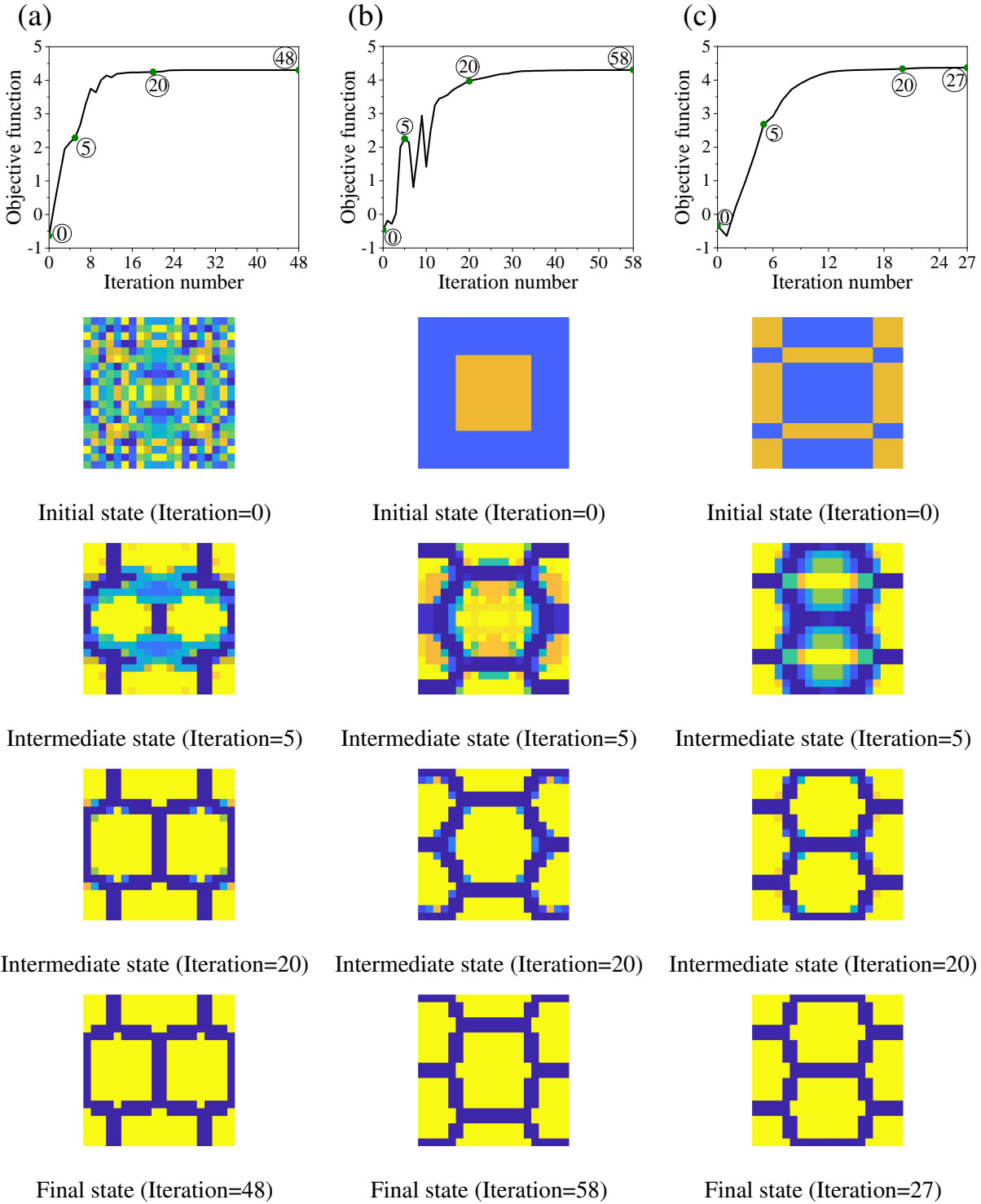


Figure 8: Optimization history and the layout evolution history of the unit cells for maximizing the band gap between 4th and 5th bands at bias electric field $e_3 = 150$ MV/m, for various initial layouts of the unit cells: (a) fully random; (b) central square fiber inclusion; and (c) fiber inclusions at multiple locations.

384 of band gaps in dielectric elastomers (Bortot et al., 2018). For this purpose, we compare the
 385 optimized designs of the unit cells and the corresponding optimized band gaps obtained using

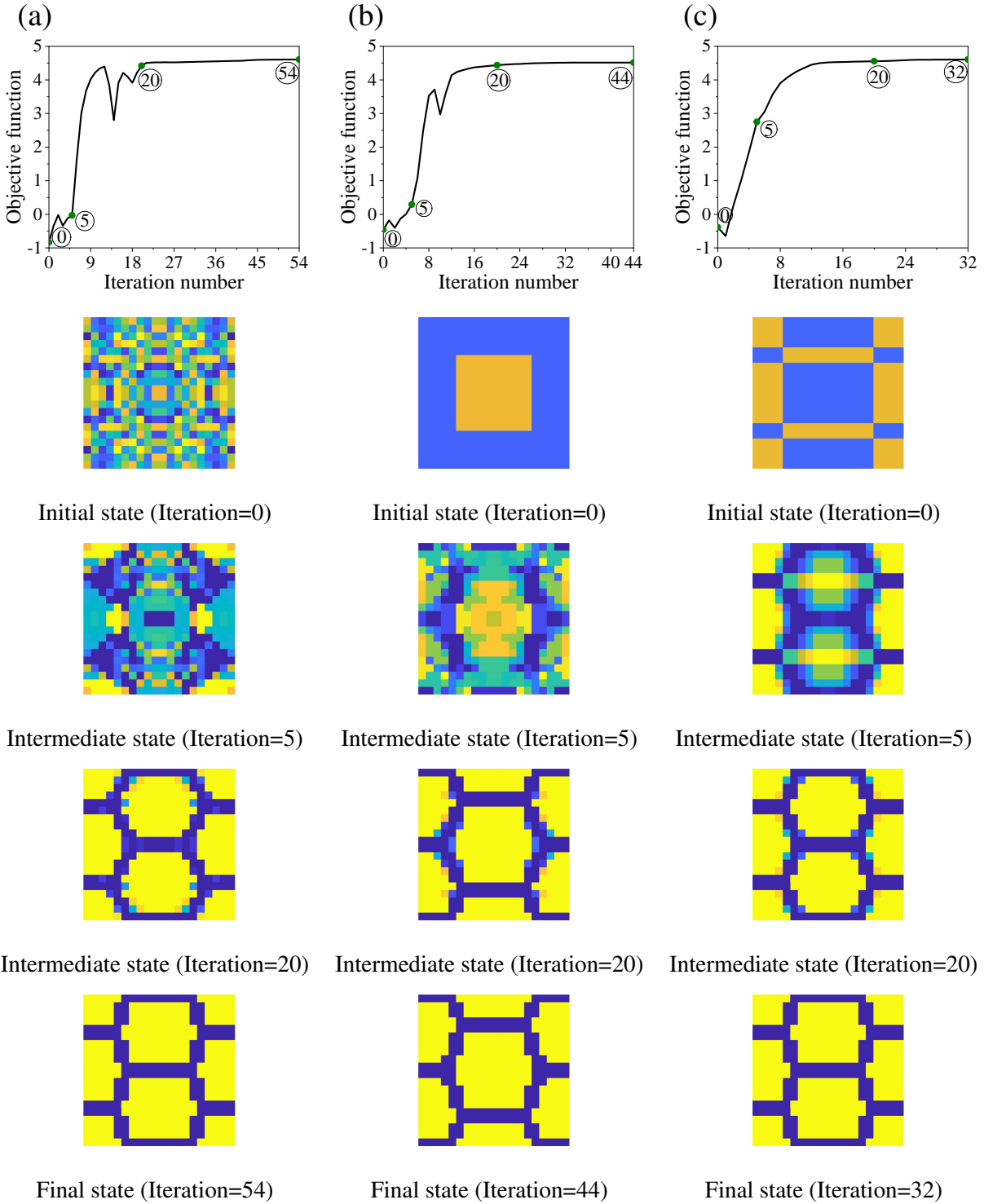


Figure 9: Optimization history and the layout evolution history of the unit cells for maximizing the band gap between 4th and 5th bands at bias electric field $e_3 = 300$ MV/m, for various initial layouts of the unit cells: (a) fully random; (b) central square fiber inclusion; and (c) fiber inclusions at multiple locations.

386 both methods of optimization. For one-to-one comparison, we consider the design structures
 387 optimized at the same mesh density i.e., 20×20 . Figures 12a and 12b show the designs of the

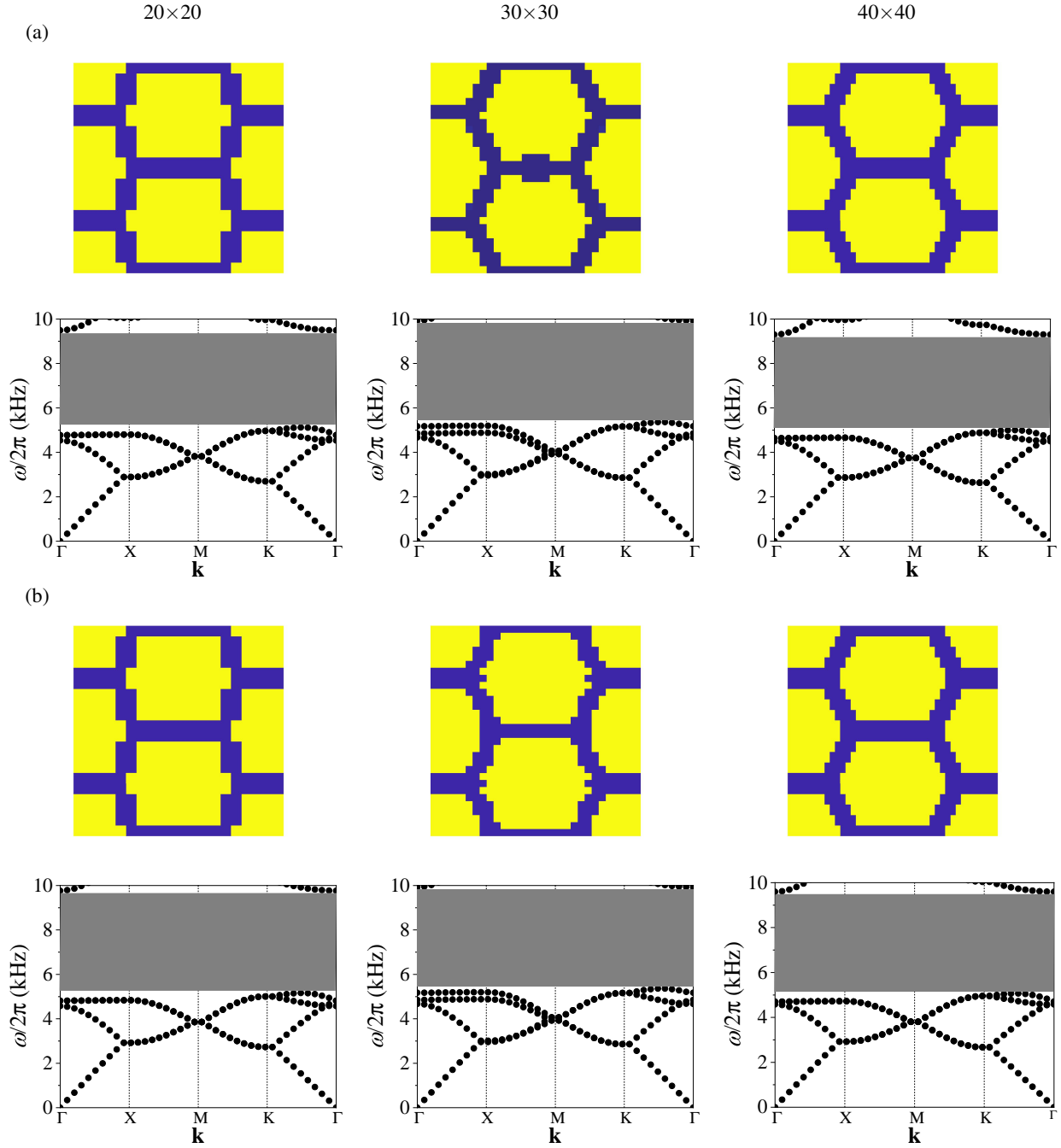


Figure 10: Effect of mesh size (left, 20×20 ; middle, 30×30 ; right, 40×40) on the optimized layouts of the unit cells for maximizing the band gap between 4th and 5th bands, when bias electric field (a) $e_3 = 150$ MV/m, and (b) $e_3 = 300$ MV/m.

388 optimized unit cell obtained using gradient-based and GA-based topology optimization methods,
 389 respectively, at bias electric field $e_3 = 150$. The fiber volume fraction for the unit cell optimized
 390 using a gradient-based optimization scheme is 0.68 and while for that optimized using GA is equal
 391 to 0.64. The band diagrams for optimized unit cells in Figs. 12a and 12b are shown in Fig. 12c.
 392 From the band diagrams, we observe the larger band gap for the unit cell optimized using the

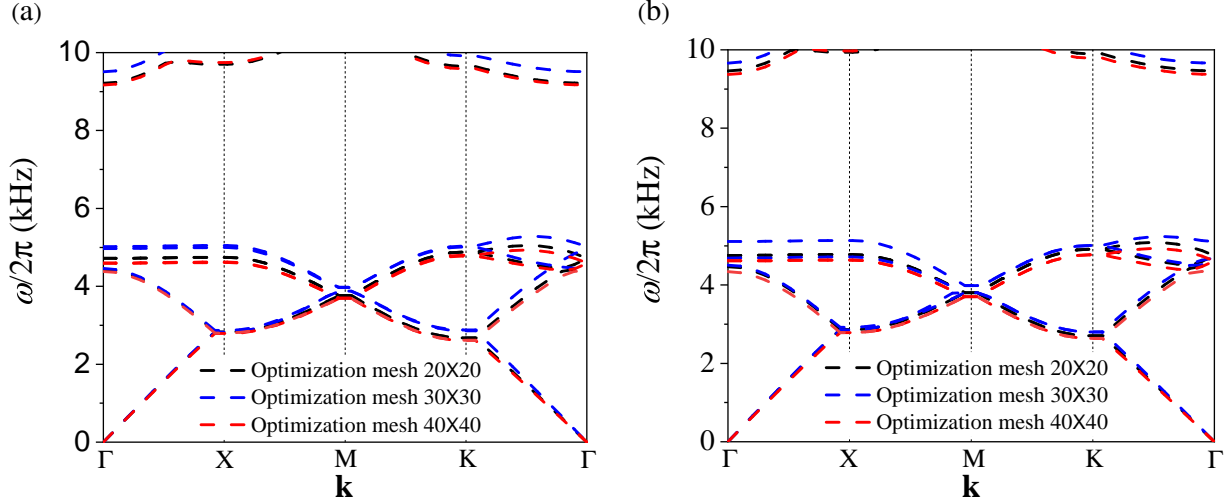


Figure 11: Comparison of the band diagrams for 120×120 mesh resolution of the unit cells optimized at 20×20 , 30×30 , and 40×40 mesh densities, (a) when bias electric field $e_3 = 150$, and (b) when bias electric field $e_3 = 300$ MV/m.

Table 5: Band gap between 4th and 5th bands at 120×120 mesh resolution for the unit cells optimized on 20×20 , 30×30 and 40×40 mesh densities.

Optimization mesh density \rightarrow	20×20		30×30		40×40	
Bias electric field (e_3) \rightarrow	150 MV/m	300 MV/m	150 MV/m	300 MV/m	150 MV/m	300 MV/m
Optimized unit cells						
Band gap at 120×120 mesh resolution	4.17 kHz	4.38 kHz	4.22 kHz	4.43 kHz	4.24 kHz	4.44 kHz

393 gradient-based formulation (4.37 kHz) in comparison to the one optimized using GA (4.13 kHz).
 394 The present approach also holds a significant computational advantage: the computational cost of
 395 the GA is higher by several orders of magnitude, and this limits the achievable design resolution.
 396 For example, Bortot et al. (2018) reported that 12,500 function evaluations were required for GA
 397 to converge in a problem with 100 design variables. Herein, these problems are solved in less
 398 than 60 design cycles, where each cycle requires a single function evaluation and the computation
 399 of gradients. The cost of computing gradients can be estimated as roughly the same as a single
 400 function evaluation. As shown above, larger design freedom can yield better band gap performance,
 401 and this can only be achieved with the gradient-based approach that easily scales to finer mesh
 402 resolutions.

403 7. Summary

404 When subjected to electric fields, dielectric elastomers undergo finite deformations and their
 405 instantaneous moduli change. These features can be exploited to electrostatically tune the width of
 406 band gaps, across which waves cannot propagate in dielectric elastomer composites.

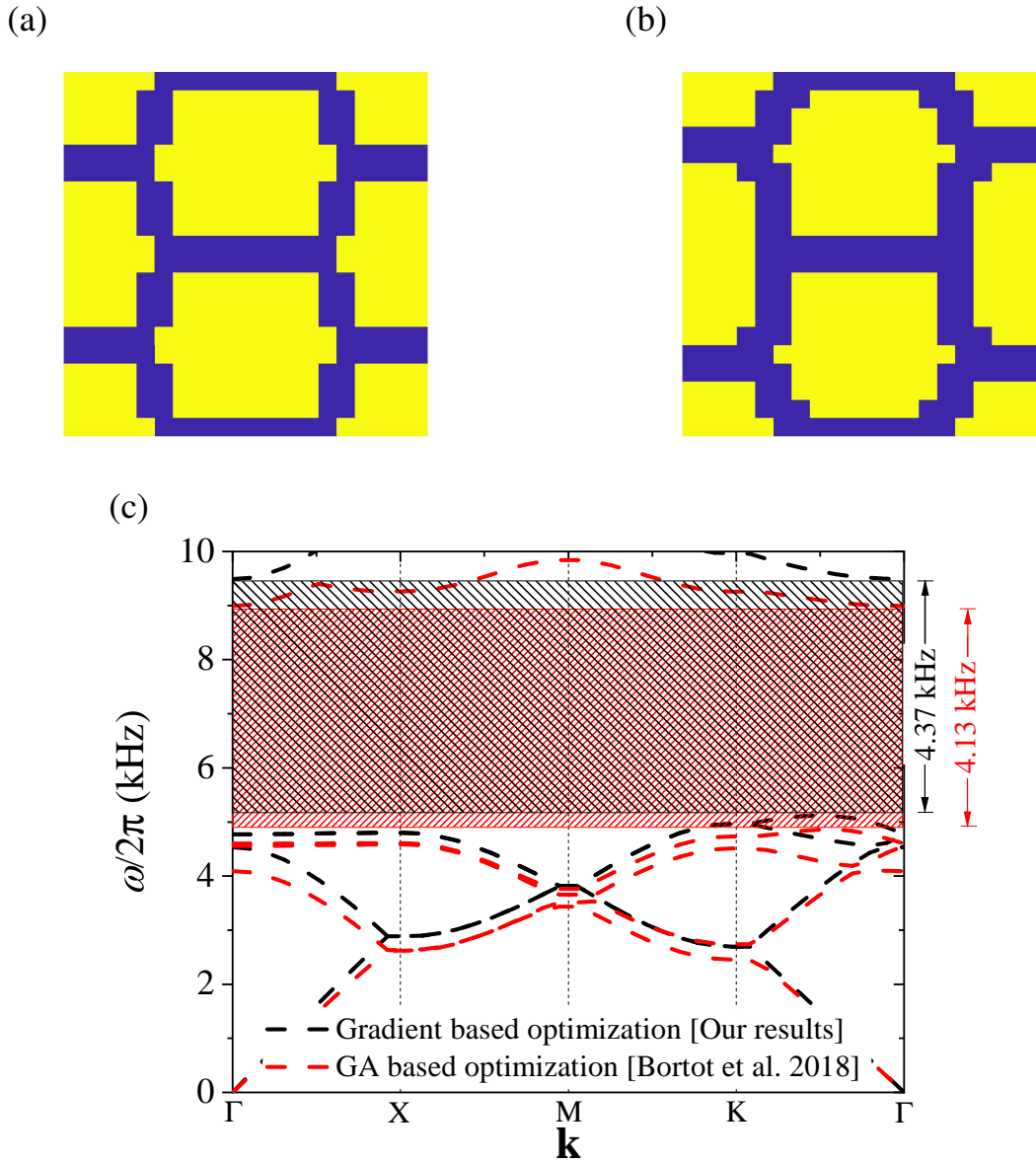


Figure 12: Designs of the unit cells optimized using (a) the gradient based optimization formulation presented in this paper and (b) a GA-based optimization method (Bortot et al., 2018). (c) Comparison of the corresponding band diagrams.

407 The width of these gaps in the actuated state is a function of the microstructure of the composite.
 408 To date, to identify optimal microstructures with wider gaps in the actuated state, topology optimization
 409 methods based on metaheuristics, specifically genetic algorithms, were used. These methods,
 410 which utilize only function evaluations without any gradient information, are limited by the computational
 411 cost that increases exponentially with the number of design variables.

412 In this work, we have developed a gradient-based topology optimization method, which utilizes
 413 information from the gradient of the objective function in order to iteratively update the design
 414 variables (Svanberg, 1987). The case study to which we have developed the method is of incremental
 415 anti-plane shear waves, propagating in a planar dielectric elastomer composite that is subjected to

416 axial electric fields (Shmuel, 2013; Getz & Shmuel, 2017; Bortot & Shmuel, 2017). To this end,
 417 we have employed a finite element formulation to obtain the eigenmodes of the linearized problem,
 418 and extract the band diagram (Benchabane et al., 2006; Li et al., 2012; Veres et al., 2013). Based on
 419 finite element formulation, we have derived and implemented a fully analytical sensitivity analysis
 420 for computing the gradient of the objective function: the width of the gap in the audible range, at
 421 two prescribed electric fields.

422 In comparison with the genetic algorithm-based method (Bortot et al., 2018), our gradient-based
 423 method not only identified microstructures with wider gaps: it also reached these microstructures
 424 in an orders-of-magnitude cheaper computational cost. Thus, the gradient-based approach easily
 425 scales to finer mesh resolutions.

426 As a potential future work, the present topology optimization framework can extended to
 427 optimize band gaps associated with in-plane motions (Getz et al., 2017); and account for the
 428 viscosity of the elastomers by the integration of viscoelastic theory (Mohajer et al., 2021; Destrade
 429 & Saccomandi, 2004; Chiang Foo et al., 2012; Hong, 2011).

430 **Acknowledgement**

431 The authors are thankful to the anonymous reviewers for their valuable input. This research
 432 was supported by the Israel Science Foundation, funded by the Israel Academy of Sciences and
 433 Humanities (Grant no. 2061/20), the United States-Israel Binational Science Foundation (Grant
 434 no. 2014358), and Ministry of Science and Technology (grant no. 880011).

435 **Appendix: Smooth formulation with approximate maximum and minimum eigenfrequencies** 436 **along the wave vector \mathbf{k}**

437 The objective function of the optimization problem in Eq. (36) is not strictly differentiable,
 438 because the \mathbf{k} -vector(s) corresponding to the maximum and minimum eigenfrequencies may change
 439 during the optimization iterations. Here, we present a topology optimization formulation in which
 440 the maximum and minimum values of eigenfrequencies along the wave vector \mathbf{k} are approximated
 441 using a p -norm function, and compare the results for one test case to those in Section 5. We examine
 442 the maximization of the band gap between the fourth and fifth bands which have a maximum
 443 optimized band gap in the audible frequency range.

444 Utilizing the standard p -norm measure (Duysinx & Sigmund, 1998; Le et al., 2010), the maximum
 445 and minimum values of the eigenfrequencies corresponding to lower and upper bands, respectively,
 446 are approximated as

$$447 \omega_{\max}^{PN} = \left(\sum_{i=1}^n (\omega_i)^p \right)^{\frac{1}{p}} ; \quad \omega_{\min}^{PN} = \frac{1}{\left(\sum_{i=1}^n \left(\frac{1}{\omega_i} \right)^p \right)^{\frac{1}{p}}}, \quad (\text{A.1})$$

447 where, p is the p -norm parameter, ω_i represents the value of the eigenfrequency corresponding to
 448 the i^{th} point along the wave vector \mathbf{k} . In this work, we took $p = 80$ and $n = 40$ points along the
 449 wave vector \mathbf{k} .

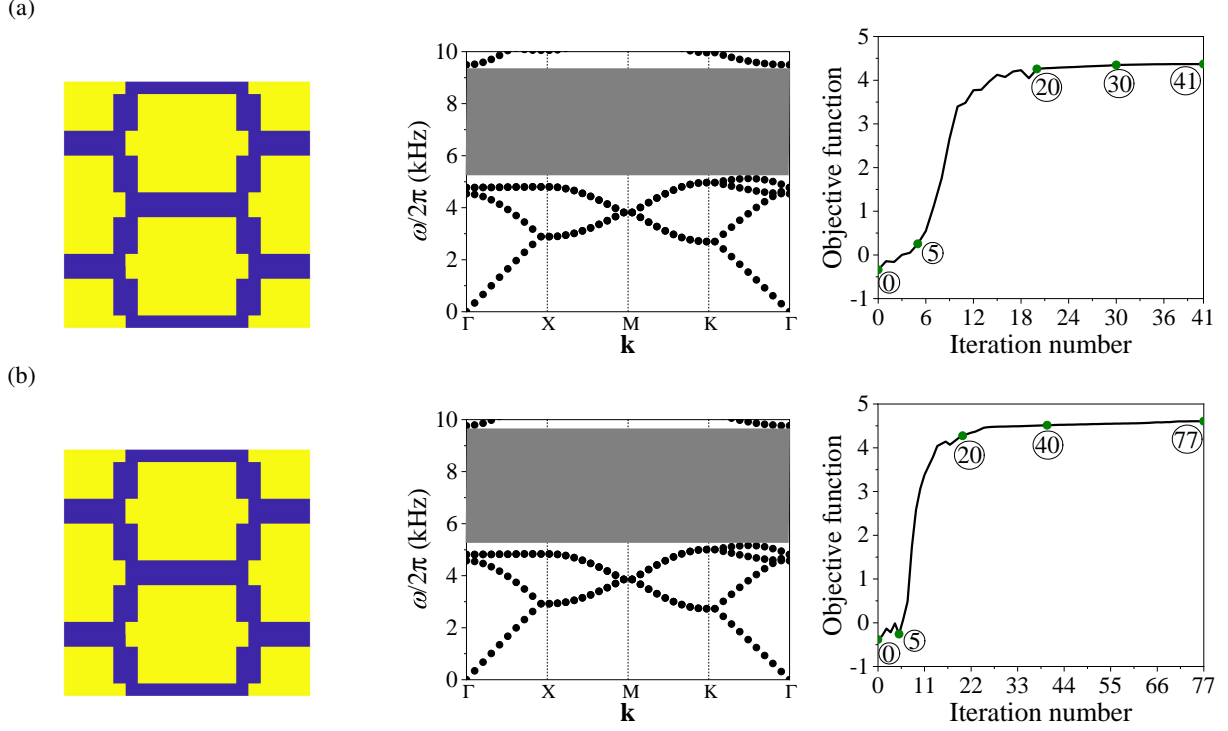


Figure 13: Unit cells (left), band diagrams (middle), and objective function history (right) when maximizing the band gap between 4th and 5th bands using the p -norm formulation, (a) when bias electric field $e_3 = 150$ MV/m, and (b) when bias electric field $e_3 = 300$ MV/m,

450 The modified version of the objective function is written as

$$f^{PN} = \begin{cases} 10 \text{ kHz} - \omega_{\max}^{PN}/2\pi & \text{if } \min \omega_{j+1}(\xi, \mathbf{k})/2\pi \geq 10\text{kHz}, \\ (\omega_{\min}^{PN} - \omega_{\max}^{PN})/2\pi & \text{if } \min \omega_{j+1}(\xi, \mathbf{k})/2\pi \leq 10\text{kHz}. \end{cases} \quad (\text{A.2})$$

451 and the sensitivities of the maximum and minimum frequencies approximated using p -norm with
 452 respect to design variable ξ_e are expressed as

$$\begin{aligned} \frac{\partial \omega_{\max}^{PN}}{\partial \xi_e} &= \left(\sum_{i=1}^n (\omega_i)^p \right)^{\frac{1}{p}-1} \left(\sum_{i=1}^n (\omega_i)^{p-1} \frac{\partial \omega_i}{\partial \xi_e} \right); \\ \frac{\partial \omega_{\min}^{PN}}{\partial \xi_e} &= \left(\sum_{i=1}^n \left(\frac{1}{\omega_i} \right)^p \right)^{-1-\frac{1}{p}} \left(\sum_{i=1}^n \left(\frac{1}{\omega_i} \right)^{p+1} \frac{\partial \omega_i}{\partial \xi_e} \right), \end{aligned} \quad (\text{A.3})$$

453 in which the derivative $\frac{\partial \omega_i}{\partial \xi_e}$ is evaluated using Eq. (39). Further, utilizing Eq. (A.3), we evaluated

454 the gradient of the modified version of the objective function $\frac{\partial f^{PN}}{\partial \xi_e}$ used for updating the design
 455 variables.

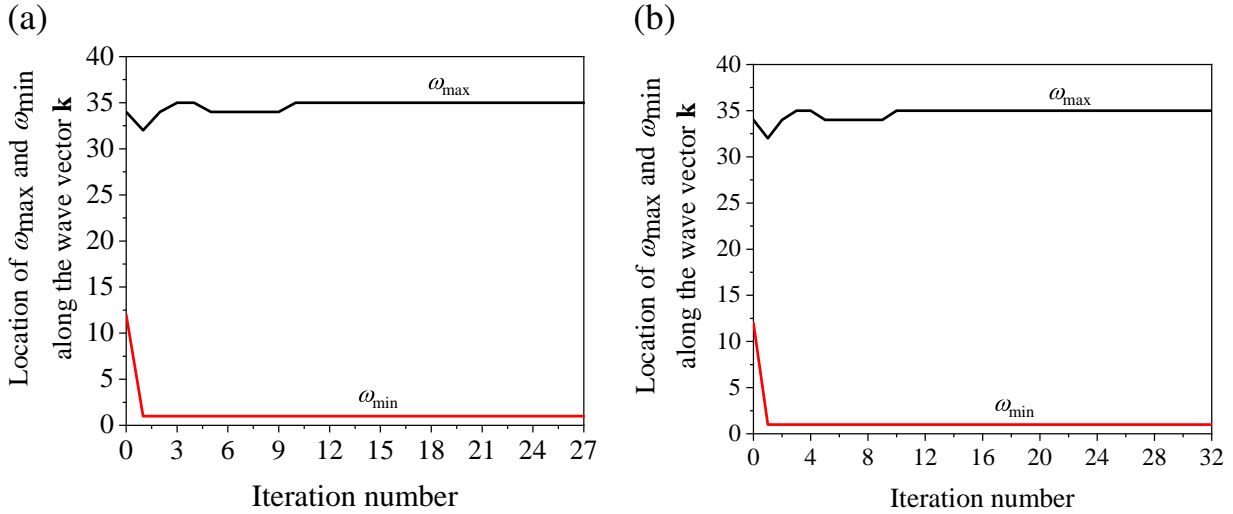


Figure 14: Variation of the location of the ω_{\max} and ω_{\min} along the wave vector \mathbf{k} , for the optimization of the band gap between 4th and 5th bands using discrete formulation (Section 5), at (a) bias electric field $e_3 = 150$ MV/m and (c) bias electric field $e_3 = 300$ MV/m.

456 The optimized layouts of the unit cell, the corresponding band diagrams, and objective function
 457 history obtained using the aforementioned p -norm formulation, for the maximization of the band
 458 gap between the 4th and 5th bands are shown in Figs. 13a and 13b, when bias electric field is equal
 459 to $e_3 = 150$ MV/m and $e_3 = 300$ MV/m, respectively. From the optimized unit cell designs, we
 460 observe that the designs are the same as those obtained using the original formulation (Figs. 8c and
 461 9c) for both values of bias electric field. In Fig. 14, we show that the location of ω_{\max} and ω_{\min} along
 462 the wave vector \mathbf{k} is almost constant same for all iterations of the non-smooth formulation. This
 463 explains why the same designs are obtained using both formulations. However, from the right panel
 464 of Figs. 13a and 13b, we observe that the optimization with p -norms takes 41 (for $e_3 = 150$ MV/m)
 465 and 77 (for $e_3 = 300$ MV/m) iterations to converge, which consumes 14 (for $e_3 = 150$ MV/m) and
 466 39 (for $e_3 = 300$ MV/m) more iterations in comparison to the non-smooth formulation (Figs. 8c and
 467 9c). Further, the computational cost of optimization with the p -norm formulation is significantly
 468 higher in comparison to the non-smooth formulation, due to the evaluation of design sensitivities
 469 or the derivatives of eigenvalues corresponding to different values of wave-vector \mathbf{k} along the first
 470 Brillouin zone.

471 References

- 472 Benchabane, S., Khelif, A., Rauch, J.-Y., Robert, L., & Laude, V. (2006). Evidence for complete
 473 surface wave band gap in a piezoelectric phononic crystal. *Physical Review E*, 73, 065601.
- 474 Bendsøe, M., & Kikuchi, N. (1988). Generating optimal topologies in structural design using
 475 a homogenization method. *Computer Methods in Applied Mechanics and Engineering*,
 476 71, 197 – 224. URL: <http://www.sciencedirect.com/science/article/pii/0045782588900862>. doi:[https://doi.org/10.1016/0045-7825\(88\)90086-2](https://doi.org/10.1016/0045-7825(88)90086-2).
- 478 Bilal, O., & Hussein, M. (2011). Ultrawide phononic band gap for combined in-plane and out-of-
 479 plane waves. *Physical Review E*, 84, 065701. doi:10.1103/PhysRevE.84.065701.

- 480 Bortot, E., Amir, O., & Shmuel, G. (2018). Topology optimization of dielectric elastomers for wide
481 tunable band gaps. *International Journal of Solids and Structures*, *143*, 262–73.
- 482 Bortot, E., & Shmuel, G. (2017). Tuning sound with soft dielectrics. *Smart Materials and*
483 *Structures*, *26*, 045028.
- 484 Chen, Y., Meng, F., Li, G., & Huang, X. (2018). Designing photonic materials with complete band
485 gaps by topology optimization. *Smart Materials and Structures*, *28*, 015025.
- 486 Chiang Foo, C., Cai, S., Jin Adrian Koh, S., Bauer, S., & Suo, Z. (2012). Model of dissipative
487 dielectric elastomers. *Journal of Applied Physics*, *111*, 034102.
- 488 De Pascalis, R., Donato, T., Ficarella, A., & Parnell, W. J. (2020). Optimal design of
489 phononic media through genetic algorithm-informed pre-stress for the control of antiplane wave
490 propagation. *Extreme Mechanics Letters*, *40*, 100896.
- 491 Deaton, J. D., & Grandhi, R. V. (2014). A survey of structural and multidisciplinary continuum
492 topology optimization: post 2000. *Structural and Multidisciplinary Optimization*, *49*, 1–38.
- 493 DeBotton, G., Tevet-Deree, L., & Socolsky, E. A. (2007). Electroactive heterogeneous polymers:
494 analysis and applications to laminated composites. *Mech. Adv. Mater. Struct.*, *14*, 13–22.
- 495 Destrade, M., & Saccomandi, G. (2004). Finite-amplitude inhomogeneous waves in mooney–rivlin
496 viscoelastic solids. *Wave Motion*, *40*, 251–62.
- 497 Dorfmann, A., & Ogden, R. (2005). Nonlinear electroelasticity. *Acta Mechanica*, *174*, 167–83.
- 498 Dorfmann, A., & Ogden, R. W. (2010). Electroelastic waves in a finitely deformed electroactive
499 material. *IMA Journal of Applied Mathematics*, *75*, 603–36.
- 500 Duysinx, P., & Sigmund, O. (1998). New developments in handling stress constraints in optimal
501 material distribution. In *7th AIAA/USAF/NASA/ISSMO symposium on multidisciplinary analysis*
502 *and optimization* (p. 4906).
- 503 Felippa, C. (2001). Introduction to finite element methods. multifreedom constraints ii (lecture
504 notes).
- 505 Gazonas, G., Weile, D., Wildman, R., & Mohan, A. (2006). Genetic algorithm optimization of
506 phononic bandgap structures. *International Journal of Solids and Structures*, *43*, 5851–66.
507 doi:10.1016/j.ijsolstr.2005.12.002.
- 508 Gei, M., Roccabianca, S., & Bacca, M. (2011). Controlling bandgap in electroactive polymer-based
509 structures. *IEEE-ASME Trans. Mechatronics*, *16*, 102–7.
- 510 Gei, M., Springhetti, R., & Bortot, E. (2013). Performance of soft dielectric laminated
511 composites. *Smart Materials and Structures*, *22*, 104014. URL: [https://doi.org/10.](https://doi.org/10.1088/0964-1726/22/10/104014)
512 [1088/0964-1726/22/10/104014](https://doi.org/10.1088/0964-1726/22/10/104014). doi:10.1088/0964-1726/22/10/104014.
- 513 Getz, R., Kochmann, D. M., & Shmuel, G. (2017). Voltage-controlled complete stopbands in
514 two-dimensional soft dielectrics. *International Journal of Solids and Structures*, *113*, 24–36.

- 515 Getz, R., & Shmuel, G. (2017). Band gap tunability in deformable dielectric composite plates.
516 *International Journal of Solids and Structures*, *128*, 11–22.
- 517 Gu, G., Zou, J., Zhao, R., Zhao, X., & Zhu, X. (2018). Soft wall-climbing robots. *Science Robotics*,
518 *3*.
- 519 Hajiesmaili, E., & Clarke, D. R. (2021). Dielectric elastomer actuators. *Journal of Applied Physics*,
520 *129*, 151102.
- 521 Halkjær, O., Sigmund, & Jensen, J. (2006). Maximizing band gaps in plate structures.
522 *Structural and Multidisciplinary Optimization*, *32*, 263–75. doi:[https://doi.org/10.](https://doi.org/10.1007/s00158-006-0037-7)
523 [1007/s00158-006-0037-7](https://doi.org/10.1007/s00158-006-0037-7).
- 524 Hedayatrasa, S., Abhary, K., Uddin, M., & Guest, J. (2016). Optimal design of tunable
525 phononic bandgap plates under equibiaxial stretch. *Smart Materials and Structures*, *25*, 055025.
526 doi:<http://dx.doi.org/10.1088/0964-1726/25/5/055025>.
- 527 Hong, W. (2011). Modeling viscoelastic dielectrics. *Journal of the Mechanics and Physics of*
528 *Solids*, *59*, 637–50.
- 529 Huang, K.-X., Shui, G.-S., Wang, Y.-Z., & Wang, Y.-S. (2020). Meta-arrest of a fast propagating
530 crack in elastic wave metamaterials with local resonators. *Mechanics of Materials*, *148*, 103497.
- 531 Huang, K.-X., Shui, G.-S., Wang, Y.-Z., & Wang, Y.-S. (2021). Enhanced fracture resistance
532 induced by coupling multiple degrees of freedom in elastic wave metamaterials with local
533 resonators. *Journal of Elasticity*, *144*, 33–53.
- 534 Hussein, M., Hamza, K., Hulbert, G., & Saitou, K. (2007). Optimal synthesis of 2d phononic
535 crystals for broadband frequency isolation. *Waves in Random and Complex Media*, *17*, 491–510.
536 doi:[10.1080/17455030701501869](https://doi.org/10.1080/17455030701501869).
- 537 Jandron, M., & Henann, D. L. (2018). A numerical simulation capability for electroelastic wave
538 propagation in dielectric elastomer composites: Application to tunable soft phononic crystals.
539 *International Journal of Solids and Structures*, *150*, 1–21.
- 540 Kashyap, K., Sharma, A. K., & Joglekar, M. M. (2020). Nonlinear dynamic analysis of aniso-
541 visco-hyperelastic dielectric elastomer actuators. *Smart Materials and Structures*, *29*, 055014.
- 542 Khurana, A., Kumar, D., Sharma, A. K., & Joglekar, M. M. (2021). Nonlinear oscillations of
543 particle-reinforced electro-magneto-viscoelastomer actuators. *Journal of Applied Mechanics*,
544 *88*, 121002.
- 545 Kim, C.-C., Lee, H.-H., Oh, K. H., & Sun, J.-Y. (2016). Highly stretchable, transparent ionic touch
546 panel. *Science*, *353*, 682–7.
- 547 Kittel, C., McEuen, P., & McEuen, P. (1996). *Introduction to solid state physics* volume 8. Wiley
548 New York.
- 549 Kornbluh, R., & Pelrine, R. (2008). Dielectric Elastomers as Electromechanical Transducers.
550 chapter High-perfo. (pp. 33–42). Elsevier, Oxford, UK.

- 551 Kushwaha, M. S., Halevi, P., Dobrzynski, L., & Djafari-Rouhani, B. (1993). Acoustic band
552 structure of periodic elastic composites. *Physical review letters*, *71*, 2022.
- 553 Kushwaha, M. S., Halevi, P., Martinez, G., Dobrzynski, L., & Djafari-Rouhani, B. (1994). Theory
554 of acoustic band structure of periodic elastic composites. *Physical Review B*, *49*, 2313.
- 555 Le, C., Norato, J., Bruns, T., Ha, C., & Tortorelli, D. (2010). Stress-based topology optimization
556 for continua. *Structural and Multidisciplinary Optimization*, *41*, 605–20.
- 557 Li, J.-B., Wang, Y.-S., & Zhang, C. (2012). Dispersion relations of a periodic array of fluid-filled
558 holes embedded in an elastic solid. *Journal of Computational Acoustics*, *20*, 1250014.
- 559 Li, W., Meng, F., Chen, Y., Li, Y. f., & Huang, X. (2019). Topology optimization of photonic and
560 phononic crystals and metamaterials: a review. *Advanced Theory and Simulations*, *2*, 1900017.
- 561 Li, Y., Huang, X., Meng, F., & Zhou, S. (2016a). Evolutionary topological design for phononic
562 band gap crystals. *Structural and Multidisciplinary Optimization*, *54*, 595–617. doi:10.1007/
563 s00158-016-1424-3.
- 564 Li, Y. f., Huang, X., Meng, F., & Zhou, S. (2016b). Evolutionary topological design for phononic
565 band gap crystals. *Structural and Multidisciplinary Optimization*, *54*, 595–617.
- 566 Liu, W., Yoon, G. H., Yi, B., Choi, H., & Yang, Y. (2020). Controlling wave propagation in one-
567 dimensional structures through topology optimization. *Computers & Structures*, *241*, 106368.
- 568 Liu, Z., Wu, B., & He, C. (2014). Band-gap optimization of two-dimensional phononic crystals
569 based on genetic algorithm and FPWE. *Waves in Random and Complex Media*, *24*, 286–305.
570 doi:10.1080/17455030.2014.901582.
- 571 Liu, Z., Wu, B., & He, C. (2016a). Systematic topology optimization of solid-solid phononic
572 crystals for multiple separate band-gaps with different polarizations. *Ultrasonics*, *65*, 249–57.
573 doi:10.1016/j.ultras.2015.09.017.
- 574 Liu, Z.-F., Wu, B., & He, C.-F. (2016b). The properties of optimal two-dimensional phononic
575 crystals with different material contrasts. *Smart Materials and Structures*, *25*, 095036.
- 576 Lu, T., Shi, Z., Shi, Q., & Wang, T. (2016). Bioinspired bicipital muscle with fiber-constrained
577 dielectric elastomer actuator. *Extreme Mechanics Letters*, *6*, 75–81.
- 578 Lu, Y., Yang, Y., Guest, J., & Srivastava, A. (2017). 3-D phononic crystals with ultra-wide
579 band gaps. *Scientific Reports*, *7*, 43407 EP -. URL: [http://dx.doi.org/10.1038/
580 srep43407](http://dx.doi.org/10.1038/srep43407).
- 581 Lustig, B., & Shmuel, G. (2018). On the band gap universality of multiphase
582 laminates and its applications. *Journal of the Mechanics and Physics of Solids*,
583 *117*, 37–53. URL: [http://www.sciencedirect.com/science/article/pii/
584 S0022509618302321](http://www.sciencedirect.com/science/article/pii/S0022509618302321). doi:<https://doi.org/10.1016/j.jmps.2018.04.008>.
- 585 Meng, F., Li, Y., Li, S., Lin, H., Jia, B., & Huang, X. (2017). Achieving large band gaps in 2d
586 symmetric and asymmetric photonic crystals. *Journal of Lightwave Technology*, *35*, 1670–6.

- 587 Mohajer, M., Zhou, J., & Jiang, L. (2021). Small amplitude rayleigh-lamb wave propagation
588 in a finitely deformed viscoelastic dielectric elastomer (de) layer. *International Journal*
589 *of Solids and Structures*, 208-209, 93–106. URL: <https://www.sciencedirect.com/science/article/pii/S0020768320303917>. doi:<https://doi.org/10.1016/j.ijsolstr.2020.10.006>.
- 592 Oliveira, J., Pinho-da Cruz, J., Andrade-Campos, A., & Teixeira-Dias, F. (2010). Stress-and strain-
593 based multifreedom constraints for periodic media optimisation. *Actas da EngOpt*, .
- 594 Ortigosa, R., & Martínez-Frutos, J. (2021). Multi-resolution methods for the topology optimization
595 of nonlinear electro-active polymers at large strains. *Computational Mechanics*, (pp. 1–23).
- 596 Ortigosa, R., Martínez-Frutos, J., Ruiz, D., Donoso, A., & Bellido, J. (2021). Density-based
597 topology optimisation considering nonlinear electromechanics. *Structural and Multidisciplinary*
598 *Optimization*, (pp. 1–24).
- 599 Pelrine, R., Kornbluh, R., Pei, Q., & Joseph, J. (2000). High-speed electrically actuated elastomers
600 with strain greater than 100%. *Science*, 287, 836–9.
- 601 Qian, X., & Sigmund, O. (2011). Isogeometric shape optimization of photonic crystals via coons
602 patches. *Computer Methods in Applied Mechanics and Engineering*, 200, 2237–55.
- 603 Quinteros, L., Meruane, V., & Cardoso, E. L. (2021). Phononic band gap optimization in truss-
604 like cellular structures using smooth p-norm approximations. *Structural and Multidisciplinary*
605 *Optimization*, (pp. 1–12).
- 606 Ren, T., Li, F., Chen, Y., Liu, C., & Zhang, C. (2020). Improvement of the band-gap characteristics
607 of active composite laminate metamaterial plates. *Composite Structures*, 254, 112831.
- 608 Sharma, A. K. (2020). Design of a command-shaping scheme for mitigating residual vibrations in
609 dielectric elastomer actuators. *Journal of Applied Mechanics*, 87.
- 610 Sharma, A. K., Arora, N., & Joglekar, M. M. (2018). Dc dynamic pull-in instability of a
611 dielectric elastomer balloon: an energy-based approach. *Proceedings of the Royal Society A:*
612 *Mathematical, Physical and Engineering Sciences*, 474, 20170900.
- 613 Sharma, A. K., Bajpayee, S., Joglekar, D. M., & Joglekar, M. M. (2017). Dynamic instability
614 of dielectric elastomer actuators subjected to unequal biaxial prestress. *Smart Materials and*
615 *Structures*, 26, 115019.
- 616 Sharma, A. K., Kumar, P., Singh, A., Joglekar, D. M., & Joglekar, M. M. (2019). Electromechanical
617 instability of dielectric elastomer actuators with active and inactive electric regions. *Journal of*
618 *Applied Mechanics*, 86.
- 619 Sharma, A. K., Sheshkar, N., & Gupta, A. (2021). Static and dynamic stability of dielectric
620 elastomer fiber composites. *Materials Today: Proceedings*, 44, 2043–7.
- 621 Shmuel, G. (2013). Electrostatically tunable band gaps in finitely extensible dielectric elastomer
622 fiber composites. *International Journal of Solids and Structures*, 50, 680–6.

- 623 Shmuel, G., & Band, R. (2016). Universality of the frequency spectrum of laminates. *J. Mech. Phys.*
624 *Solids*, 92, 127–36. doi:<http://dx.doi.org/10.1016/j.jmps.2016.04.001>.
- 625 Shmuel, G., & Debotton, G. (2012). Band-gaps in electrostatically controlled dielectric laminates
626 subjected to incremental shear motions. *J. Mech. Phys. Solids*, 60, 1970–81. doi:10.1016/j.
627 *jmps.2012.05.006*.
- 628 Shmuel, G., Gei, M., & DeBotton, G. (2012). The Rayleigh-Lamb wave propagation in
629 dielectric elastomer layers subjected to large deformations. *Int. J. Non-Linear. Mech.*, 47, 307–
630 16.
- 631 Shmuel, G., & Pernas-Salomón, R. (2016). Manipulating motions of elastomer films by
632 electrostatically-controlled aperiodicity. *Smart Materials and Structures*, 25, 125012.
- 633 Sigmund, O., & Maute, K. (2013). Topology optimization approaches. *Structural and*
634 *Multidisciplinary Optimization*, 48, 1031–55.
- 635 Sigmund, O., & Søndergaard Jensen, J. (2003). Systematic design of phononic band-gap materials
636 and structures by topology optimization. *Philosophical Transactions of the Royal Society of*
637 *London. Series A: Mathematical, Physical and Engineering Sciences*, 361, 1001–19.
- 638 Su, Y., Chen, W., & Destrade, M. (2019). Tuning the pull-in instability of soft dielectric
639 elastomers through loading protocols. *International Journal of Non-Linear Mechanics*,
640 113, 62–6. URL: [https://www.sciencedirect.com/science/article/pii/](https://www.sciencedirect.com/science/article/pii/S0020746218306863)
641 [S0020746218306863](https://www.sciencedirect.com/science/article/pii/S0020746218306863). doi:[https://doi.org/10.1016/j.ijnonlinmec.2019.](https://doi.org/10.1016/j.ijnonlinmec.2019.03.008)
642 [03.008](https://doi.org/10.1016/j.ijnonlinmec.2019.03.008).
- 643 Su, Y., Wu, B., Chen, W., & Lü, C. (2018). Optimizing parameters to achieve giant deformation
644 of an incompressible dielectric elastomeric plate. *Extreme Mechanics Letters*, 22, 60–8.
645 doi:<https://doi.org/10.1016/j.eml.2018.05.004>.
- 646 Suo, Z., Zhao, X., & Greene, W. H. (2008). A nonlinear field theory of deformable dielectrics.
647 *Journal of the Mechanics and Physics of Solids*, 56, 467–86.
- 648 Svanberg, K. (1987). The method of moving asymptotes—a new method for structural
649 optimization. *International journal for numerical methods in engineering*, 24, 359–73.
- 650 Vatanabe, S. L., Paulino, G. H., & Silva, E. C. (2014). Maximizing phononic band gaps in
651 piezocomposite materials by means of topology optimization. *The Journal of the Acoustical*
652 *Society of America*, 136, 494–501.
- 653 Veres, I. A., Berer, T., & Matsuda, O. (2013). Complex band structures of two dimensional
654 phononic crystals: Analysis by the finite element method. *Journal of Applied Physics*, 114,
655 083519.
- 656 Wang, Y.-F., Wang, Y.-Z., Wu, B., Chen, W., & Wang, Y.-S. (2020). Tunable and active phononic
657 crystals and metamaterials. *Applied Mechanics Reviews*, 72.

- 658 Xie, L., Xia, B., Liu, J., Huang, G., & Lei, J. (2017). An improved fast plane wave expansion
659 method for topology optimization of phononic crystals. *International Journal of Mechanical*
660 *Science*, *120*, 171–81. doi:[http://dx.doi.org/10.1016/j.ijmecsci.2016.11.](http://dx.doi.org/10.1016/j.ijmecsci.2016.11.023)
661 023.
- 662 Yang, X., & Kim, Y. Y. (2018). Topology optimization for the design of perfect mode-converting
663 anisotropic elastic metamaterials. *Composite Structures*, *201*, 161–77.
- 664 Yi, G., Shin, Y. C., Yoon, H., Jo, S.-H., & Youn, B. D. (2019). Topology optimization for phononic
665 band gap maximization considering a target driving frequency. *JMST Advances*, *1*, 153–9.
- 666 Yi, G., & Youn, B. D. (2016). A comprehensive survey on topology optimization of phononic
667 crystals. *Structural and Multidisciplinary Optimization*, *54*, 1315–44.
- 668 Zhang, G., & Gao, X.-L. (2018). Elastic wave propagation in 3-d periodic composites: Band gaps
669 incorporating microstructure effects. *Composite Structures*, *204*, 920–32.
- 670 Zhang, X., Xing, J., Liu, P., Luo, Y., & Kang, Z. (2021). Realization of full and directional band
671 gap design by non-gradient topology optimization in acoustic metamaterials. *Extreme Mechanics*
672 *Letters*, *42*, 101126.
- 673 Zhao, X., Hong, W., & Suo, Z. (2007). Electromechanical hysteresis and coexistent states in
674 dielectric elastomers. *Physical review B*, *76*, 134113.
- 675 Zhu, F., Wu, B., Destrade, M., & Chen, W. (2020). Electrostatically tunable
676 axisymmetric vibrations of soft electro-active tubes. *Journal of Sound and Vibration*,
677 *483*, 115467. URL: [https://www.sciencedirect.com/science/article/pii/](https://www.sciencedirect.com/science/article/pii/S0022460X20302996)
678 [S0022460X20302996](https://www.sciencedirect.com/science/article/pii/S0022460X20302996). doi:<https://doi.org/10.1016/j.jsv.2020.115467>.
- 679 Ziser, Y., & Shmuel, G. (2017). Experimental slowing of flexural waves in dielectric elastomer
680 films by voltage. *Mech. Res. Commun.*, *85*, 64–8. URL: [http://www.sciencedirect.](http://www.sciencedirect.com/science/article/pii/S0093641317302197)
681 [com/science/article/pii/S0093641317302197](http://www.sciencedirect.com/science/article/pii/S0093641317302197). doi:[https://doi.org/10.](https://doi.org/10.1016/j.mechrescom.2017.08.005)
682 [1016/j.mechrescom.2017.08.005](https://doi.org/10.1016/j.mechrescom.2017.08.005).